OH* AND CH* CHEMILUMINESCENCE AND OH PLIF IMAGING STUDIES IN SPHERICALLY EXPANDING FLAMES

A Thesis

by

TYLER THOMAS PASCHAL

Submitted to the Office of Graduate and Professional Studies of
Texas A&M University
in partial fulfillment of the requirements for the degree of

MASTER OF SCIENCE

Chair of Committee,	Waruna D. Kulatilaka
Committee Members,	Eric L. Petersen
	Rodney Bowersox
Head of Department,	Andreas A. Polycarpou

May 2019

Major Subject: Mechanical Engineering

ABSTRACT

The work performed in this research is aimed at developing two repeatable methods for imaging spherically expanding flames operated in a constant volume flame vessel. The first, passive diagnostic method imaged the chemiluminescence emission of radicals OH^* and CH^* in a range of flame equivalence ratios (0.7–1.3) at a rate of 2 kHz, and the data were used to measure the laminar flame speed via the same image processing used for measuring laminar flame speed using conventional schlieren imaging experiments. The optical filters for OH^* and CH^* (315 ± 15 nm and 434 ± 17 nm, respectively) applied to the high-speed, intensified imaging system created volume-integrated species-specific images of spherically expanding flames. The radial profiles of Abel inverted images showed a clear intensity peak near the edge of the flame corresponding to the flame front. The full-width-at-half-maximum (FWHM) in these radial profile curves estimated a thickness of the radical zone at the edge of the flame, and these thicknesses were on the order of 1mm, and their time histories were evaluated. The second experimental method introduced a laser excitation source for single-shot planar laser-induced fluorescence (PLIF) of the hydroxyl radical (OH). The PLIF apparatus was optimized to create a repeatable timing sequence to open the camera exposure gate over a single laser pulse, and the resulting images showed two-dimensional spatial distribution of ground-state OH in the methane-air flames. Quantitative OH calibration was performed using a Hencken calibration burner to compute a number-density to pixel-intensity ratio for each equivalence ratio, and this ratio was applied to the images to show absolute OH number densities in the 2-D plane

of the flame. The images show a time-series of the propagation of a stoichiometric, methane-air flame and the change of OH concentration at a fixed flame radius across a range of equivalence ratios (0.7–1.3). Radial profiles of OH reveal differences between lean and rich flame radical gradients. Proof-of-principle OH PLIF images of a turbulent flame is also presented. Future experiments will use this data for validating detailed chemical kinetics models of spherically expanding flames.

ACKNOWLEDGMENTS

I would like to thank my advisor, Dr. Kulatilaka, for funding, support, and guidance throughout my research. Without Dr. Kulatilaka and the members of the Optical Diagnostics and Imaging Laboratory, this project would not have been possible.

I would also like to thank my committee members Dr. Eric Petersen and Dr. Rodney Bowersox for their guidance. Also Carl Johnson who manages the Turbomachinery Laboratory at Texas A&M, and members of Petersen research group owe a big thanks. Without the facilities provided by the Turbomachinery Laboratory, this work would not have been performed.

Special thanks go to my family and fiancée who continually supported me and pushed me to work at my best potential throughout my years of study and during the writing of this thesis. This accomplishment would not have been possible without them.

Thank you all and thank you to those who also provided support but were not directly mentioned.

CONTRIBUTORS AND FUNDING SOURCES

Contributors

This work was supervised by a thesis committee consisting of Professors, Waruna Kulatilaka and Eric Petersen of the J. Mike Walker ’66 Department of Mechanical Engineering and Professor Rodney Bowersox of the Department of Aerospace Engineering.

Mattias Turner was responsible for preparing and conducting the flame experiments within the vessel. Mr. Turner was also responsible for the flame speed analyses of the chemiluminescence images. Pradeep Parajuli contributed to the experiments by conducting chemiluminescence imaging experiments and providing key assistance in developing the PLIF laser system as well as conducting PLIF experiments. Post-doctoral researcher Yejun Wang provided key insight from his experience in combustion diagnostics and helped conduct the calibration experiments.

All other work conducted for the thesis (or) dissertation was completed by the student independently.

Funding Sources

This work was made possible in part by the Defense Threat Reduction Agency (DTRA) under Grant Number HDTRA1-16-1-0031, and the United States Department of Energy, National Energy Technology Laboratory through NETL-Penn State University Coalition for Fossil Energy Research, contract number DE-FE0026825. Its contents are solely the responsibility of the authors and do not necessarily represent the official views of the above agencies.

TABLE OF CONTENTS

Page

LIST OF FIGURES

Page

CHAPTER I

INTRODUCTION

Combustion diagnostics is a way to experimentally develop chemical kinetics models and characterize flames in various combustion devices. Machines that depend on developments from combustion research include but are not limited to internal combustion engines, gas turbines, and jet engines. These dynamic environments and many others contain combustion reactions with high heat release at a wide range of temperatures and pressures. Different gas mixtures will react differently under these conditions, effecting overall combustion efficiency and pollutant formation. Characterizing the behavior of certain mixtures in specific initial conditions is useful for developing the models for the combustors. The introduction of lasers to probe experimental combustion apparatuses is a way to non-intrusively probe flames to take measurements related to species number densities, temperature, pressure, flow dynamics, and other parameters that characterize a flame. To develop a successful and repeatable apparatus for applications in combustion diagnostics requires previous knowledge of many different areas such as optics and lasers, chemical kinetics, thermodynamics, fluid mechanics.

This thesis will describe in full detail the background, methods, and results of two separate combustion diagnostic experiments in canonical configurations of spherically expanding flames commonly used to obtain the laminar and turbulent flame speeds. The first of the two experiments is high-speed chemiluminescence imaging that takes advantage of the natural light emission from electronically-excited combustion

radicals. Several approaches of analyses for flame speed as well as chemical species time histories were performed to develop an understanding of the evolution of spherically expanding, laminar flames. The second set of experiments, hydroxyl radical planar laser-induced fluorescence (OH PLIF), introduced the application of an excitation source: a tunable dye laser. As described in detail within the second half of this thesis, OH PLIF reveals spatially resolved ground-state OH number densities which is one step further than that of chemiluminescence, albeit with added experimental difficulties. Such measurements are imperative for validating complex combustion mechanism in variety of hydrogen and hydrocarbon fuel mixtures under realistic engine operating conditions.

Chapter II presents a review of literature related to the topics at hand. A brief overview is made of the mechanics of electronic excitation of radicals present in combustion reactions, followed by a review of the various experiments used in laminar flame studies. Chapter III details the apparatus configuration for high-speed chemiluminescence imaging, describes the process of performing Abel inversion of LOS-integrated images, and presents the results from the experiments. Chapter IV describes the apparatus for single-shot planar laser-induced fluorescence of OH in the same spherically expanding flames as in Chapter III, followed by a presentation and discussion of the data obtained in these experiments. The conclusions of the data and suggestions to improve the experiments in future work are made in Chapter V.

CHAPTER II

LITERATURE REVIEW

1. Chemiluminescence Imaging of Combustion Radicals

a. Electronic Excitation of Radicals

Energy transfer in a chemical reaction occurs as bonds break and new bonds are formed, and atoms and molecules collide with one another, and molecules formed in the intermediate reactions that contain an unpaired valence electron that are affected by this energy transfer. These unstable molecules referred to as radicals, and although they have short lifetimes, they are present for enough time to collide with nearby particles and absorb some kinetic energy. The kinetic energy is absorbed by the unpaired valence electron, which enters an electronically excited state. After some time, that electron releases the energy as it transitions back to ground state, emitting a photon. Figure 1 illustrates this excitation and emission process.

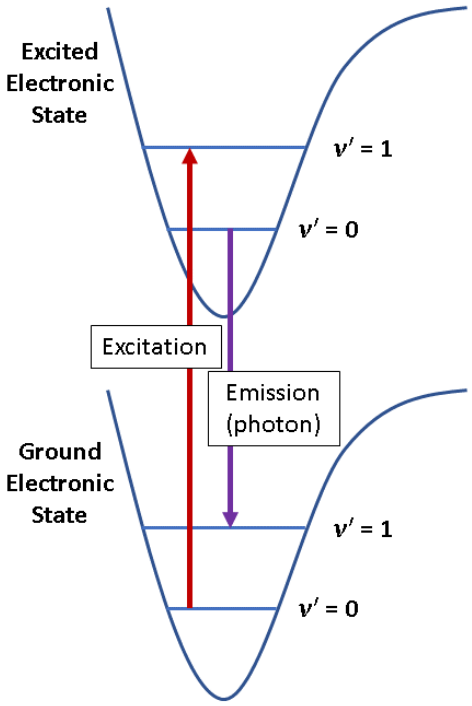

Figure 1: Representation of electronic excitation and resulting chemiliuminescence of a diatomic radical such as OH or CH.

The quantum, electronic and ro-vibrational energy levels of a molecule are discrete, and numerous studies have been conducted regarding their quantization [1–3]. Work done by Bennett et al. evaluated the lifetime of electronically excited OH denoted by OH*, and their results concluded that OH* resides in the first excited state for 0.99 μs extrapolated to zero pressure. This information is important when considering imaging gate widths, as discussed in the experimental section of the thesis. Typically, these electronic transitions emit photons in the ultraviolet band, ranging from 10–400 nm wavelength, but some weak emissions are in the visible range over 400 nm. Photon energies of emissions are characteristic of radicals, and knowing their wavelengths

allows imaging of specific species. Also measuring the total spectra can be used to determine the electronically-excited species present in a reaction.

b. Laminar Flame Studies

In combustion research, there are an array of experimental configurations used to produce laminar flames including the burner-stabilized flat flame, the constant-volume, spherically expanding flame, and the counterflow flame [4–6]. The propagation rate of a laminar flame is critical for developing the fundamentals of flame kinetics models. Although there are multiple techniques for measuring the laminar flame speed, each technique has its own advantages and limitations, and each are applicable within discrete pressure ranges that typically determine the technique necessary for a given study. A survey of these techniques was conducted by Egolfopoulos et al. [4].

Low-pressure flame studies less than one-tenth of an atmosphere have been conducted with flat burner-stabilized flames, because flame thickness at these pressures is large enough for a probe to measure temperature and species concentrations. Instabilities and heat loss are induced by the probe, but these effects can subsequently be corrected. At higher, sub-atmospheric pressures the burner-stabilized flames are used to measure the flame speed via the heat flux method [7]. The first successful study of this kind was conducted by Van Marren et al., and they measured the laminar burning velocity of methane/air approximately 6 cm/s lower than ~41 cm/s reported in previous studies, revealing the effects of heat loss and stretch that should be accounted for [8]. Other fuels used in the same study showed similar comparison with previous data, that previous measurements overestimate the adiabatic laminar flame speed.

At pressures slightly greater than atmospheric, the counterflow flame apparatus has been used for measuring the laminar flame speed by the LDV technique [9,10]. The counterflow twin flame uses two flames impinging on each other with a nitrogen co-flow to reduce effects from the surrounding environment. Non-combusting seed particles such as alumina particles are added to the flow, and a laser doppler velocimetry setup tracks the particle flow within the combusting gases. This technique is useful for measuring limits of ignition and extinction, species concentration, and laminar burning velocity [11]. Unfortunately, heat loss effects prevent experimenters from recording meaningful data in sub-atmospheric pressures.

At atmospheric pressure and higher pressures up to tens of atmospheres, the constant-volume vessel can produce spherically expanding flames from a quiescent premix of gases. Spherically expanding flames are created within a constant-volume vessel by creating a mixture of fuel and oxidant within the vessel, and the equivalence ratio and initial pressure are controlled by pressure gauges. When the proper mix is achieved, a spark is created in the center of the vessel, and from this spark the flame front propagates through the fluid to the vessel walls. Because the mixture is homogenous and quiescent, the flame propagation is the same in all directions from the center, resulting in a spherically expanding flame. The laminar flame speed is measured via a schlieren optical apparatus that images the density gradient within the vessel through windows in the vessel walls. A sample of images that result from a spherically expanding flame propagation experiment with schlieren imaging is provided in Figure 2. Images like these are then processed with an edge detection algorithm, which detects the edge of the flame

in each image to calculate the change in radius over time. After correcting for stretch and multiplying by the density ratio of the unburned and burned gases, the laminar flame speed is calculated.

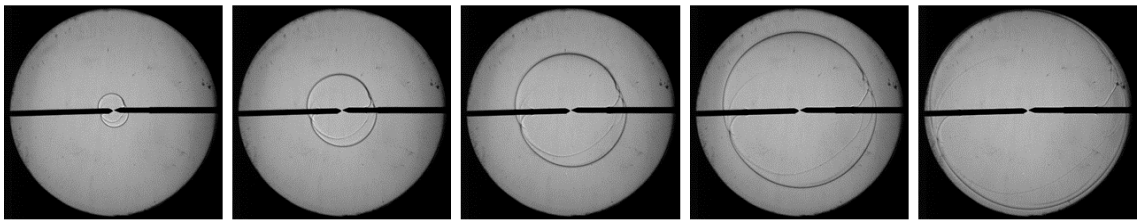

Figure 2: Set of schlieren images for a 1 atm mix of methane/air (ϕ = 1.1). Sequential images are separated in time by 5 ms.

The limit of spherically expanding experiments is in the sub-atmospheric regime due to the increase in ignition radius, but the constant-volume vessel can achieve pressures unattainable by the stagnation and burner-stabilized flames [12–19]. Other effects in spherically expanding flames are due to buoyancy and thermal cellular instabilities. In slower flames, gas density ratio can be great enough such that the spherical flame translates upward through the unburned gas mixture due to buoyancy, clearly affecting the laminar flame speed calculation. In high-pressure experiments, flames appear to have wrinkles that are recognized as thermal cellular instabilities, and in flames where this instability is great, edge detection prevents laminar flame speed calculation. In more recent work, the constant-volume vessel has been made configurable for turbulent flow with the introduction of stirring fans. Adding fans allows the constant-volume vessel to produce flames in a combination of low to high pressure and laminar or turbulent flow of known turbulent intensity. This is desirable for generating conditions like those in real combustors.

This work sought to use the spherically expanding flame apparatus in a constant-volume flame vessel to image the chemiluminescence of OH* and CH* of methane/air mixtures at atmospheric initial pressure and temperature. Recently, several papers produced by this experimental group highlight the studies involved in this thesis using high-speed chemiluminescence imaging of OH^* and CH^* radicals to demonstrate the purpose of multi-dimensional combustion studies using species-specific images [20,21]. These data were used to measure laminar flame speed using a similar approach as in commonly used schlieren imaging. Additional combustion characteristics were obtained using species-specific chemiluminescence data such as spatial analysis of radical distribution within the spherical flame. A limitation of the chemiluminescence method is that they are line-of-sight (LOS) integrated, and as a result, no absolute measurements can be made of number densities of the radical species under investigation, especially when the flame becomes fully turbulent and lacks any axisymmetric nature.

2. Planar Laser-Induced Fluorescence Imaging of Hydroxyl (OH PLIF)

The investigation of fundamental laminar flames and controlled, repeatable, turbulent combustion conditions representative of real-world combustors are two capabilities of constant-volume flame vessels commonly used in combustion studies. One way to overcome the limitation of spatial averaging effects in chemiluminescence imaging would be to image the flame radicals such that the data are spatially resolved, which can be accomplished with the introduction of a laser-sheet to probe the flame. Planar laser-induced fluorescence (PLIF) began with the purpose of imaging two-dimensional (2D) fields of species number densities, temperature, pressure, and flame

structure characteristics [22,23]. Compared to other optical diagnostics, PLIF has an advantage of strong signal levels and quantitative single-shot imaging. Most other laser diagnostics in combustion are LOS-integrated and/or point measurements that possibly mask critical features of the flame, specifically fluid dynamic effects and combustion instabilities. Previously, PLIF has been used to investigate symmetry of OH in turbulent combustion in hydrogen-fueled engines [24], three-dimensional temperature field measurement in water [25], and near-field imaging studies in high-pressure, cryogenic jet flames [26], among many others.

Commonly investigated species in PLIF experimental studies include OH, NO, CH, and tracers in reacting and non-reacting flows [27]. The most common species studied in PLIF applications is OH [23,26,28–30]. With the introduction of precise, tunable Ng:YAG/dye laser systems and better understanding of electronic states in combustion radicals, experimenters have multiple options when choosing excitation transitions for specific studies. Factors that can affect the choice of excitation band include the available excitation source, laser and signal absorption affects, and spectral separation between the excitation and emission bands. The most common excitation for OH in combustion studies has been the $A \leftarrow X$ (1,0) band near 282 nm [31–34].

Most of the work referenced in this paper studied OH PLIF in a range of laminar and turbulent combustion. The present work is focused on exploring a repeatable apparatus for studying the fundamental, spherically expanding, laminar flames as well as well-characterized turbulent flames inside a constant volume vessel. Experimental considerations are discussed including mobilizing the laser system, probing inside a

constant-volume combustion vessel, and timing the laser, ignition, and imaging system in a repeatable manner. Precise mixtures of methane and air were burned in a spherically expanding flame vessel, and single-shot OH-PLIF images were recorded. Thorough details are provided on the experimental apparatus for future experiments. Data obtained in this experiment will provide a time-history of OH radicals in laminar flames, and absolute number densities are compared for flames of varying equivalence ratios. The constant-volume vessel includes the optional stirring fans, and representative OH profiles in selected turbulent flame are also presented.

CHAPTER III

OH* AND CH* CHEMILUMINESCENCE IMAGING STUDY

1. Experimental Apparatus

Observing the propagation of a spherically expanding flame via imaging through a narrow spectral band required an ultra-sensitive imaging device that can acquire data at a high repetition rate. Flames are generated inside a high-pressure vessel with a stagnant, combustible gas mixture ignited at the center. The chemiluminescence experimental apparatus used in these studies is shown in Figure 3. Shown in the upper right is the turbulent flame speed vessel (TFSV) where the combustion events take place. The imaging system used to record the expanding flame at 2 kHz is also shown in Figure 6. These experiments were operated remotely from outside of the walls that enclosed the combustion vessel.

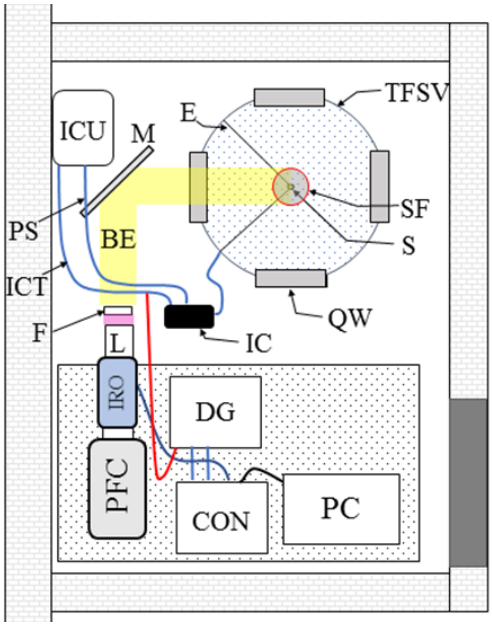

BE Broadband Flame Emission
CON Intensifier Controller
DG Delay Generator
E Electrode (x2)
F Narrow Bandpass Filter (OH* or CH*)
IC Ignition Coil
ICT Ignition Coil Trigger (5 V)
ICU Ignition Control Unit
IRO Intensifier
L UV Lens
M Mirror (Silver)
PFC High-speed Cam
PS Ignition Coil Power Supply (12 V)
QW Quartz Window (x4)
S Spark
SF Spherical Flame
TFSV Turbulent Flame Speed Vessel

Figure 3: Spherically expanding chemiluminescence imaging experimental apparatus.

a. Constant-Volume Flame Vessel

The laminar, spherically expanding combustion events occurred within the TFSV described in Morones et. al [35]. The TFSV is a stainless-steel cylinder of 407 mm in height and 356 mm in diameter, which can produce laminar and turbulent flames at a wide range of equivalence ratios and initial pressures. An external valve system was used to fill the vessel with fuel and oxidizer to create a combustible mixture at a range of pressures from sub-atmospheric up to 10 atm. The optional fans provide the ability to stir the mixture and create known turbulence levels, but during the present laminar flame studies, these fans were removed from the vessel. Two copper electrodes fixed at the vessel wall pointing towards the center were used to ignite the mixture. Because the ignition takes place at a small volume in the center of the vessel, the flame expands symmetrically and radially outwards from the point of ignition. A 40-kV, light-duty-truck ignition coil was used to generate a short, high-voltage spark across the tips of the electrodes after receiving a 5 V TTL trigger pulse from the ignition control unit (ICU). Four orthogonal quartz windows, 127 mm diameter, placed around the circumference of the vessel were used as optical ports to image the reaction and transmit the laser beams. Figure 4 below shows the TFSV in the experimentation cell.

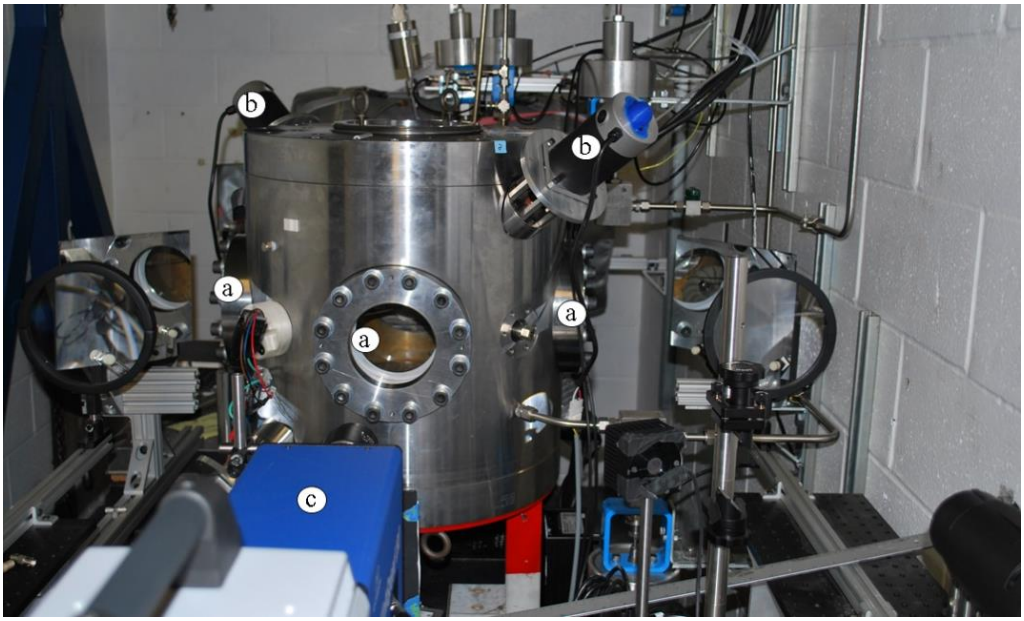

Figure 4: The Turbulent Flame Speed Vessel. Notable features of the vessel are its (a) observation windows and (b) stirring fans. Object (c) is the imaging system that will be discussed later.

b. *High-Speed, Intensified Imaging System*

The flame propagation to the edge of the window (130 mm flame diameter) of most fuels occurs within the first 150 ms of combustion. These flame speeds required a high-speed camera to image this flame propagation: the Photron Fastcam SA-Z. This CMOS detector has the capability to image up to a frame rate of 2.1 MHz with reduced resolution, however, full resolution image frame rate of 2 kHz was sufficient for current experiments. With an image taken every 0.5 µs, any given combustion resulted in between 60 and 300 images. This camera was chosen for its high-speed capabilities, but it required coupling with a device that could amplify the weak chemiluminescence signals and a detector sensitive to ultraviolet light.

A high-speed external image intensifier, namely the LaVision High-Speed Intensified Relay Optics (HS-IRO), S20 intensifier was mounted in front of the high-speed camera to create a signal that could be detected by the CMOS detector. The photocathode in the S20 intensifier functions with greater than 15% quantum efficiency for the short spectral bands around OH* and CH* emission. Electrons are produced by photons impacting the photocathode, and those electrons pass through a micro-channel plate (MCP). The micro-channel plate has a variable voltage applied to it which corresponds to the user-set gain value, which controls the amount by which the electrons are amplified. Electrons that leave the MCP then impact a phosphor plate that produces photons as it is impacted by electrons. The result is an amplification of photons that leave the intensifier and enter the high-speed CMOS detector. A photomultiplier tube functions with three main components. Figure 5 below is an illustration representing the intensifying system inside the HS-IRO device.

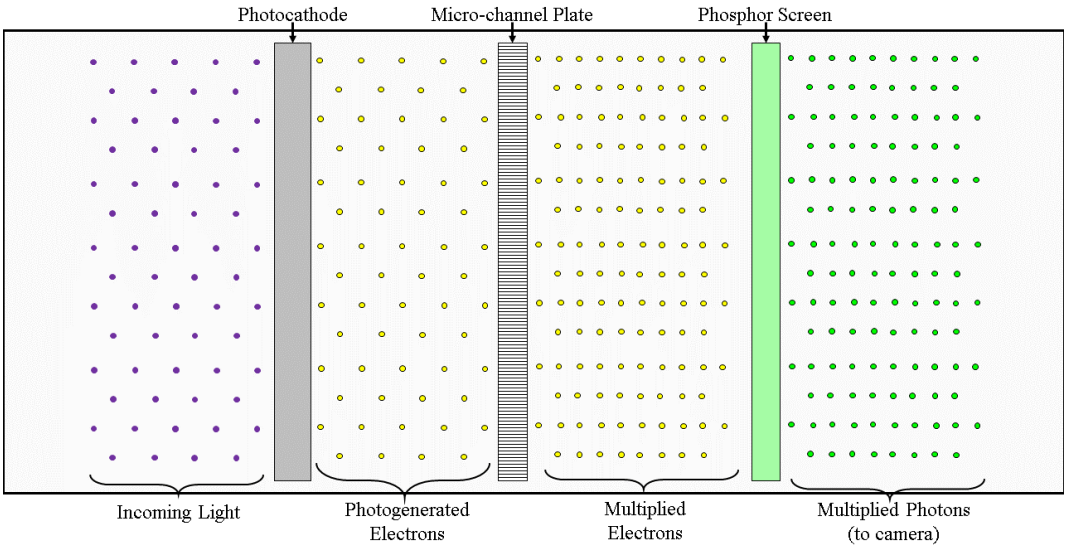

Figure 5: Schematic representing LaVision HS-IRO intensifier system.

The intensifier, controlled via LaVision software DaVis, has a variable gain setting that can be changed from experiment to experiment. This capability is important, because each the intensity of the imaged wavelength is dependent upon flame equivalence ratio (ϕ) and the species observed. Generally, OH* is of higher intensity than CH*, and their intensities reach a maximum with temperature, which corresponds to peak flame speed. As a result, the intensifier gain for each (ϕ, species) pair is different, and a limitation of this is that absolute data between experiments, being on different intensity scales, cannot be directly compared.

Using a coupler, the intensifier was mounted to the front of the high-speed camera, thus creating a system that amplifies the photons emitted by chemiluminescence and translating them into a wavelength that the CMOS detector is sensitive to. Although this intensifier is optimized for ultraviolet light, due to the weak signal from single-species chemiluminescence, it was best to improve the signal-to-noise ratio. An ultraviolet-transmitting lens (Bernhard Halle Nachfolger GmbH., ultraviolet, 400 mm lens) was used to collect the emission light into the HS-IRO. In front of this lens, a Semrock Brightline® bandpass filter was mounted resulting in a selected wavelength band of light entering the ultraviolet lens. Using these filters enabled species-specific imaging, and the respective filters are referred to by the species they observe: OH* (315 $\pm$ 15 nm) and CH* (434 $\pm$ 17 nm). With each experiment, the required filter was applied to observe either total chemiluminescence, OH*, or CH*. Of course, no filter was applied to observe total chemiluminescence. All of these components (high-speed camera, intensifier, lens, filter) make up the imaging system, and a photograph of this setup is

shown in Figure 6. The front end of this system can also be seen as it is looking at the vessel window in Figure 4.

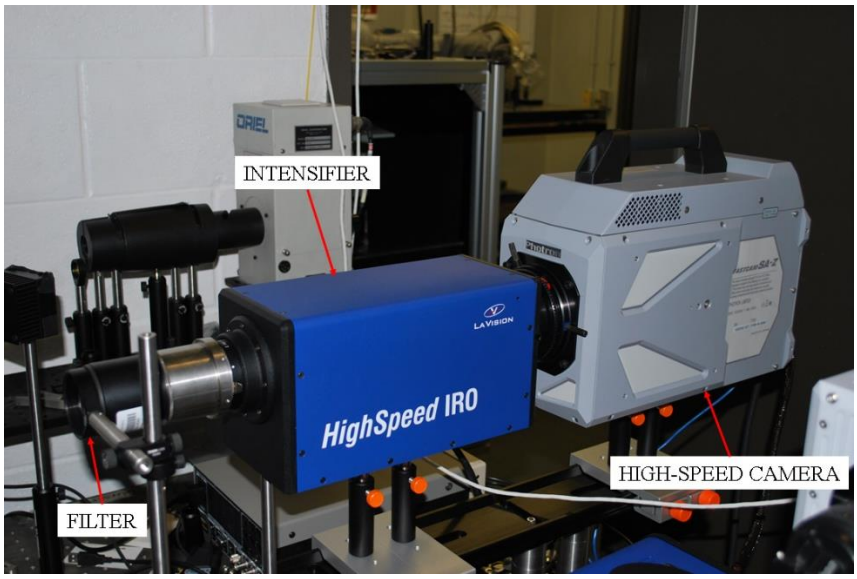

Figure 6: Chemiluminescence imaging system.

With the two-dimensional images that result from these experiments, it is important to image a scale, because this enables calculation of absolute dimensions in post-processing. To achieve this, the intensifier was set to long gate width with low gain (<10%), and an object of known, precise dimensions was imaged. In the case of the image shown in Figure 7, the image shows a set of concentric rings, each 0.25" thick. In post-processing, this image is used to measure the pixel density. In this case, the pixel density of this 1024 x 1024-pixel image is 6.68 pixels-per-millimeter. Pixel density was used to calculate the laminar flame speed and the thickness of the radical zone. At first, the pixel density was measured by moving a computer mouse over the observed location of an edge (between the bright and dark circles in Figure 7) to roughly locate the pixel location of the greatest intensity gradient. This method was clearly unreliable, and

therefore the same Canny edge detection package used in flame speed calculation was used to detect the edges the circles used for scaling.

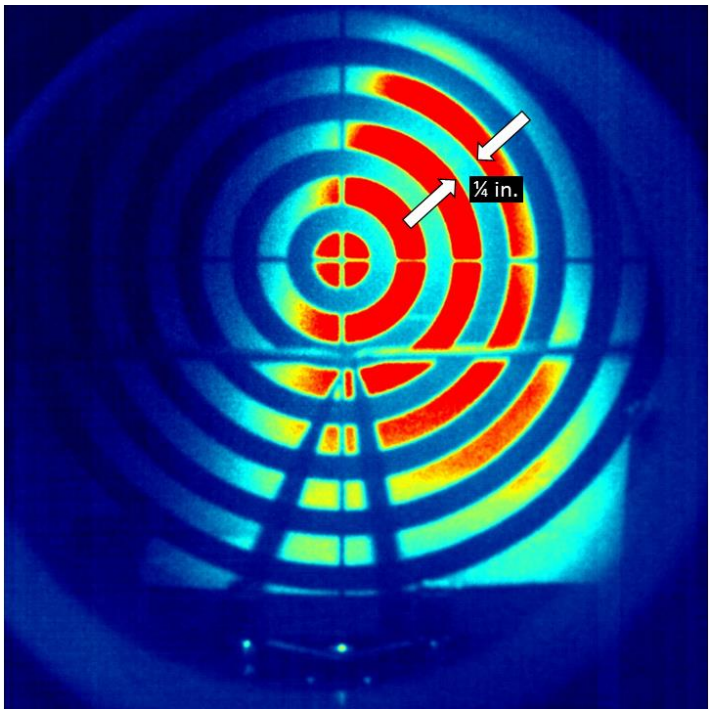

Figure 7: Image used for measuring scale/pixel density.

c. Integration and Timing

There are two characteristics of these spherically expanding flames that, when observed by the intensifier, could cause damage to the intensifier. Proper testing and safe imaging of these events enabled the use of a repeatable timing system that protected the intensifier while allowing it to image the spherically expanding flame without losing necessary data. The first of these two was the relatively bright spark that occurred across the electrode tips. The decay time of the spark was repeatable, and as a result the intensifier gate was delayed constantly at 13.35 ms, creating enough time for the bright ionized gases to decay to a level safe for the intensifier. After the flame grew in diameter greater than that of the windows, it propagated to the vessel walls and reflected into the

vessel, creating an increase in chemiluminescence signal in the entirety of the vessel. At the gain levels necessary to image the spherical chemiluminescence signal, this event was potentially damaging to the intensifier. Between these two events, the propagation of the spherical flame was imaged for the measurement of laminar flame speed, as there was no information before or during the spark and during or after the late flame events usable for laminar flame speed calculations. Figure 8 is an illustrated of the imaging timeline with respect to the main sequence of combustion events.

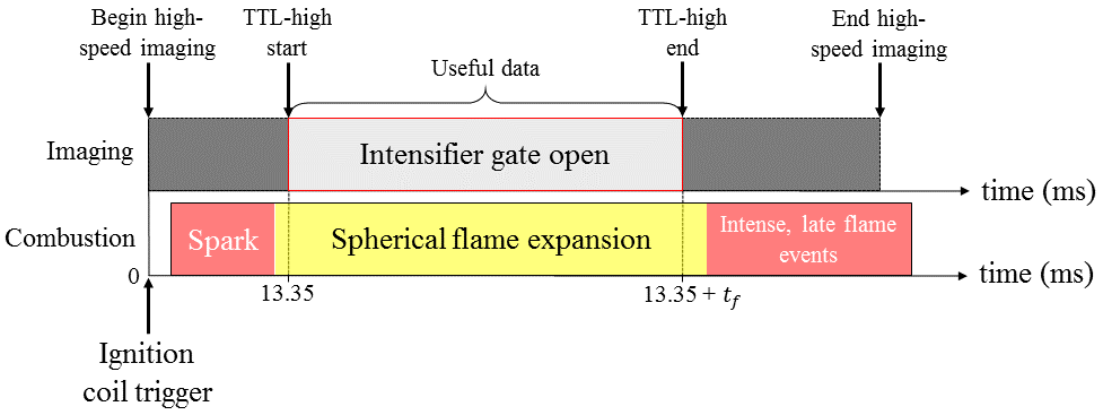

Figure 8: Event timeline for both combustion and chemiluminescence imaging.

Each experimental run was started by filling the vessel with fuel and oxidizer to the required partial pressures corresponding to a given ϕ. The initial total pressure for the laminar flame speed experiments was 760.0 ± 0.05 Torr, although other experimental cases can be performed at higher initial pressures. Meanwhile, the imaging system was set up with the necessary parameters including frame rate (2 kHz), initial delay (13.35 ms), HS-IRO gain, and image duration. Gain was varied based on the strength of the chemiluminescence signal, which is a function of ϕ. Image duration was another variable

setting, but this was dependent on the flame speed, which is a function of ϕ. The desired optical filter was placed in front of the intensifier's ultraviolet lens. Finally, the camera system and delay generator were armed to receive trigger inputs, and the experiment was initiated from a separate room away from the TFSV assembly enclosed by thick steel-reinforced concrete walls. This process was repeated three times at each ϕ, for the three wavelength bands: total chemiluminescence (no filter), OH^* (315-nm filter), and CH^* (434-nm filter). The value of ϕ was varied between 0.7 and 1.3 in increments of 0.1, yielding a of total 21 runs.

2. Results and Discussion

a. Laminar Flame Speed

The data resulting from the chemiluminescence imaging experiments are a sequence of images of the spherically expanding flame front. In the current study, sequential images are separated by 500 μs , and the data were acquired at 2 kHz and a 65 μs gate width. The three datasets in Figure 9 are the results of three separate experimental runs, and they are a sample that is representative of the rest of the data. Any given data set resulted in anywhere between 60 and 200 images. In the images the black, horizontal lines are the electrodes where the spark is generated, which is also consistent with the camera view illustrated in Figure 3. Inside the false-color blue circle are the combustion products, and within the black background area surrounding the circle is the mixture of unburned gases. After the combustible mixture is ignited across the electrode tips, the flame propagates radially outwards from the point of ignition, until it reaches the vessel walls. The signal from each image corresponds to the applied

wavelength filter that is denoted for each row of images. The data between different wavelengths were acquired using different gain settings of the intensifier.

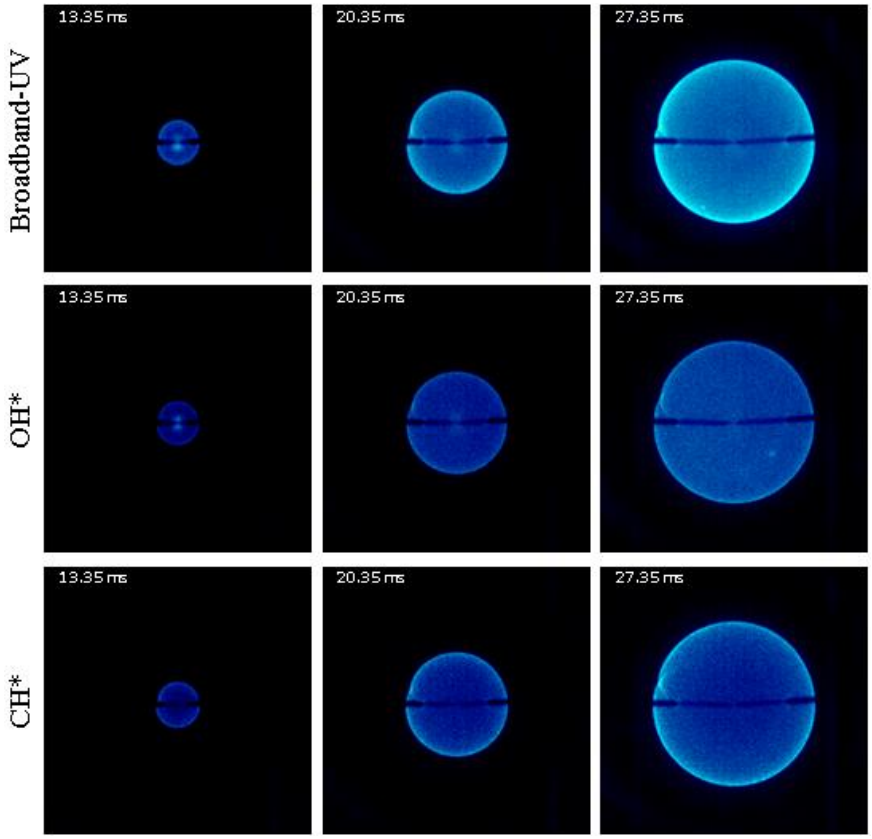

Figure 9: A Sample series of time-resolved chemiluminescence images. For this experiment, ϕ = 1.1 was held constant. The frame size of each image is approximately 15.2 x 15.2 cm. From [21]; reprinted by permission of the American Institute of Aeronautics and Astronautics, Inc.

These images are visually similar to schlieren data used in laminar flame speed calculation [36]. Laminar flame speed calculations are traditionally performed using a series of high-speed images of density gradients that illustrate the propagation of the flame over a known time. Image processing algorithms detect the flame edge (the

prominent circle of the flame) and calculate $\frac{dr}{dt}$ of the stretched, burned flame. Through the reactant and product density ratio and flame kinetics, the stretched, burned flame speed is converted to a value representing an unstretched, unburned mixture. Because of the similarities to the schlieren data, it is possible that chemiluminescence data could be used to calculate laminar flame speed, as discussed in detail by Turner et. al. [20].

b. Radical Zone Thickness

i. Inverse Abel Transform of LOS-integrated Images

As stated previously, chemiluminescence imaging is limited in that it is LOS-integrated, meaning that absolute information concerning population distribution of the observed radical cannot be obtained with the raw images. The inverse Abel transform is a derivative-based numerical method used to construct a 2D slice of a 3D object from an image of integrated, axisymmetric data. There are different methods by which to compute this transform, but all are sensitive to noise [37]. The most efficient of the methods is the Hansen and Law method [37]. These experiments used the Python package PyAbel, which contains an array of image processing functions with the purpose of evaluating the forward and inverse Abel transforms [38]. The inverse Abel transform was used to study the time-history of the thickness of the radical zone.

One requirement of the Abel transform function is that the object within the image has a center that corresponds to the pixel center. The electrode tips were not perfectly centered within the image. This resulted in an off-center image that was centered in post-processing. Also, due to buoyancy effects, lean flames were lifted upwards over time. The application of the "abel.tools.center.center_image" function

created flame-centered images that were input into the inverse Abel transform function. With the current edition of the PyAbel package, there were three functional centering methods: center of mass, convolution, and slice. Center of mass functions by finding the center of mass according to pixel intensity. This works well for the two-electrode images. The convolution method takes a convolution of two projections along each axis. The third method, slice, compares adjacent angular slices, of size dr, for symmetry based on the radial location of peak intensity in each slice. Figure 10 provides an example of the various centering methods for a lean flame ($\phi = 0.7$, OH^*). In this case, the electrodes are off-center, and the flame has risen such that the horizontal centerline is out of plane with the electrodes. Upon inspection, center of mass and convolution provide a usable centering method for the Abel inversion.

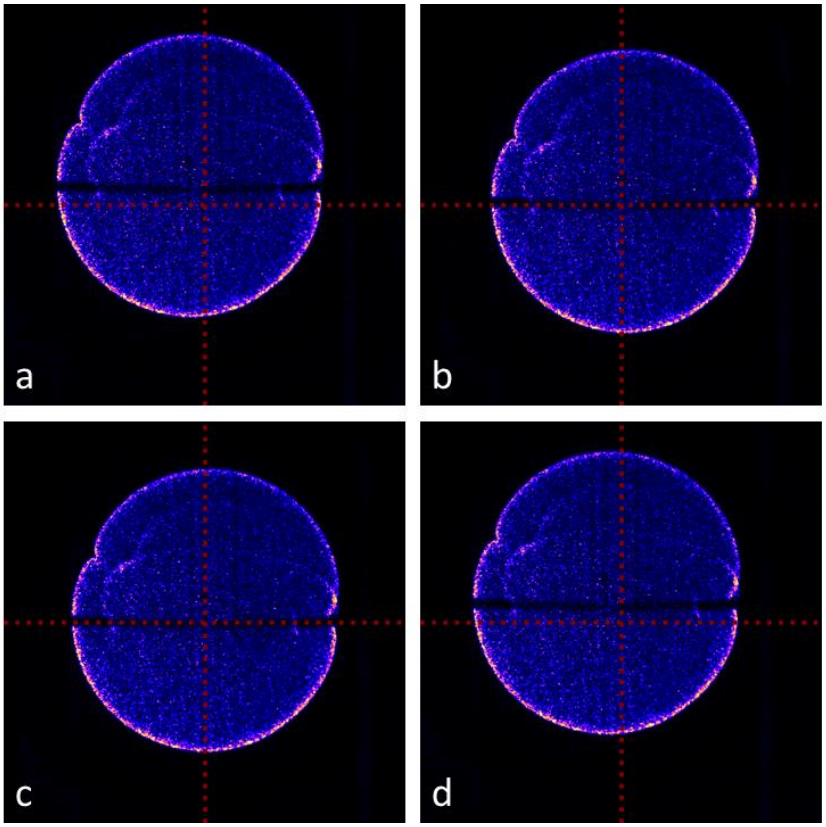

Figure 10: (a) Original, off-center image. (b) Center of mass by pixel intensities. (c) Convolution of x and y axes. (d) Slices compared for symmetry. Intersection of red lines marks the image center.

Although center of mass and convolution appeared to produce the same results, an angular integration of the methods highlighted the difference between their outputs. The angular integration was done with a built-in function within the PyAbel package, and it is called “abel.tools.vmi.angular_integration”. The function returned the intensity profile as a function of the radius [38]. Figure 11 illustrates the angular integration profiles for the images shown in Figure 10. It became clear that convolution produced the sharpest intensity profile, implying that it centers the near-circular flame image objectively better than the other two methods. Now, a method was established by which

to center images before performing the inverse Abel transform. This method was repeated for other images to solidify confidence in the convolution method.

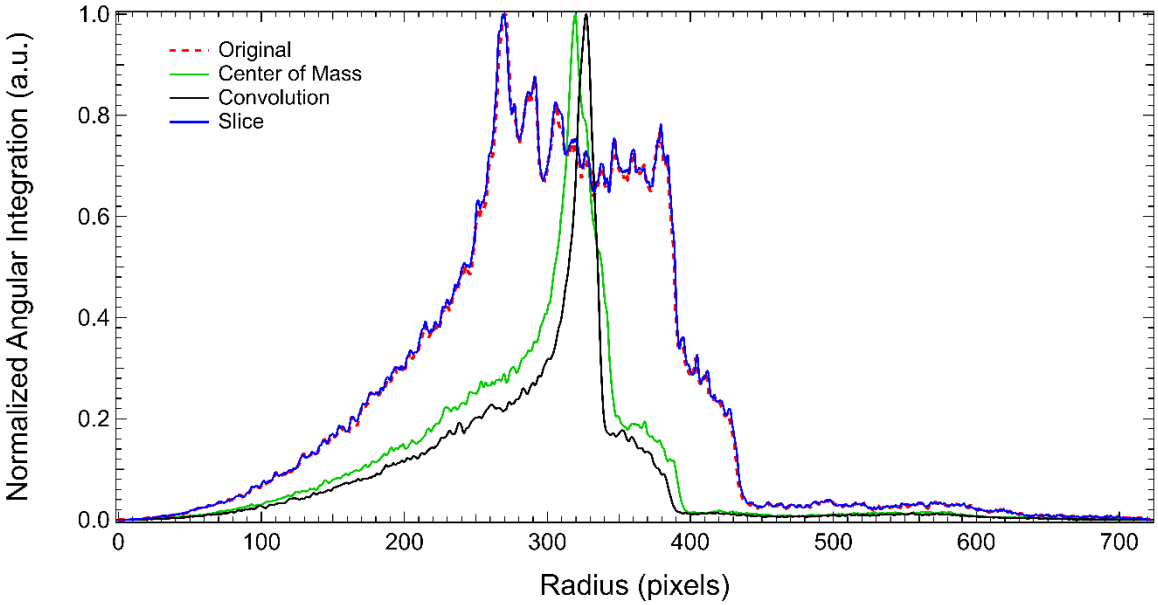

Figure 11: Angular integration profiles for the centering methods: center of mass, convolution, and slice. The raw image is included for absolute comparison.

Before moving forward with this analysis, a certain discretion is to be made. A separate set of chemiluminescence experiments were performed through a different port of the combustion vessel, resulting in images where the electrodes were one behind the other on the left side of the image. Convolution centering was useful for the images where the electrodes were symmetric and visible on both sides, however, for other chemiluminescence experiments, convolution did not provide usable images. Therefore, a similar study was conducted for the asymmetric images to verify a usable centering method for the Abel inversions.

With an established centering method, convolution-centered images were Abel inverted by the "transform" method of the "abel.Transform" class, i.e.

"abel.Transform(*image*).transform". There were various Abel transform methods: BASEX, Direct, Hansen-Law, Lin-Basex, Two Point, Three Point, Onion Peeling (Dasch), Onion Peeling (Bordas), Polar Onion Peeling, and Fourier-Hankel [38]. Due to the incompleteness of the PyAbel package, the Hansen-Law method was performed for these images. Hansen-Law transform was preferred for its speed and low noise levels. Python implementation of this method required specifying both the method name as well as the direction: "forward" or "inverse". As stated earlier, the forward transform constructs a LOS-integrated image from a slice of a 3D, axisymmetric volume, and the inverse transform generates a slice of the 3D volume from a LOS-integrated image. Figure 12 shows pre- and post-inverted images by the Hansen and Law inversion. Figure 12b is the derivative of the integrated image, Figure 12a, resulting in a 2D slice of OH^* within the flame volume. Inverted images resulted in a high-contrast flame edge with a bright line in the vertical center of the flame. The exact cause of this vertical line is currently unknown, but it is certainly an artifact of the numerical inversion algorithm. Flame features originally masked by low contrast became more visible after inversion, such as wrinkles close to the edge of the flame.

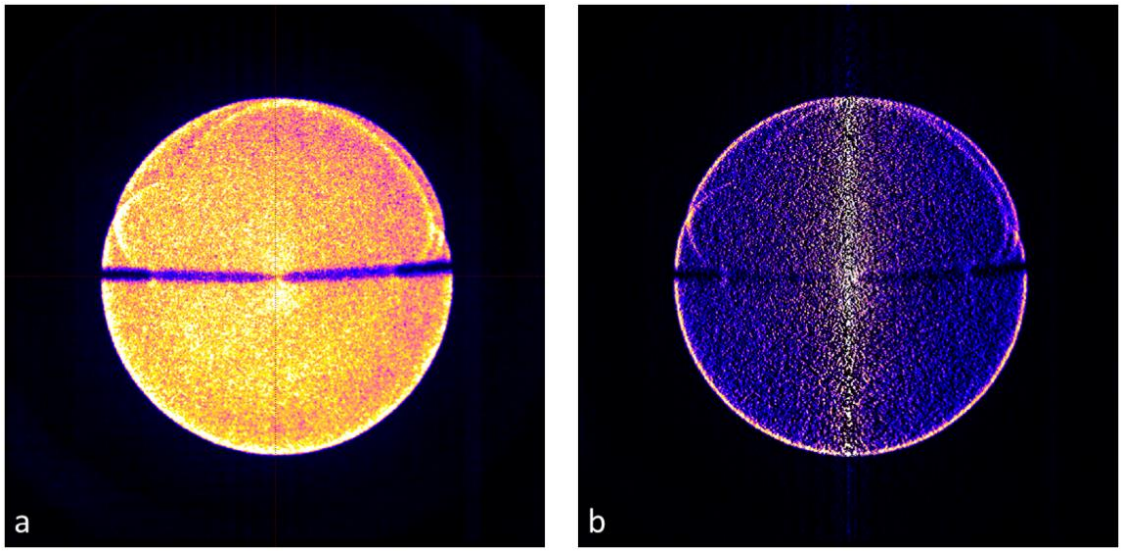

Figure 12: (a) Stoichiometric, methane-air flame, OH* chemiluminescence image (1024x1024 pixels, 6.68 pixels-per-mm). (b) Hansen and Law Abel inverted image of (a).

An angular integration from the flame center to the edge of the image quantified the differences between the two images, shown in Figure 13. There was a slight but noticeable shift in the profile peaks, where the peak signal of the inverted image was slightly further from the flame center compared to the original image. The shift can likely be attributed to the reduction in signal inside the flame edge as a result of the inversion, and the uncorrected image has a peak intensity that is slightly inside the circle edge. As the radius increases, the effect from signal integration was reduced, and the inversion effect was weakest at the edge of the flame. This could provide an explanation for the shift in signal peaks. The result of the inversion was as expected: the inverted signal was less than 20% of the peak within most of the flame volume, and there was a rapid increase in signal 3 mm before the peak. This rapid signal increase was expected: because OH^* is a marker of the reaction zone, the population density of OH^* should increase near the surface of the flame volume. From this angular integration of the Abel inversion, the

full-width-at-half-maximum (FWHM) was calculated by interpolation between the two points on either side of 0.5 in the y-values.

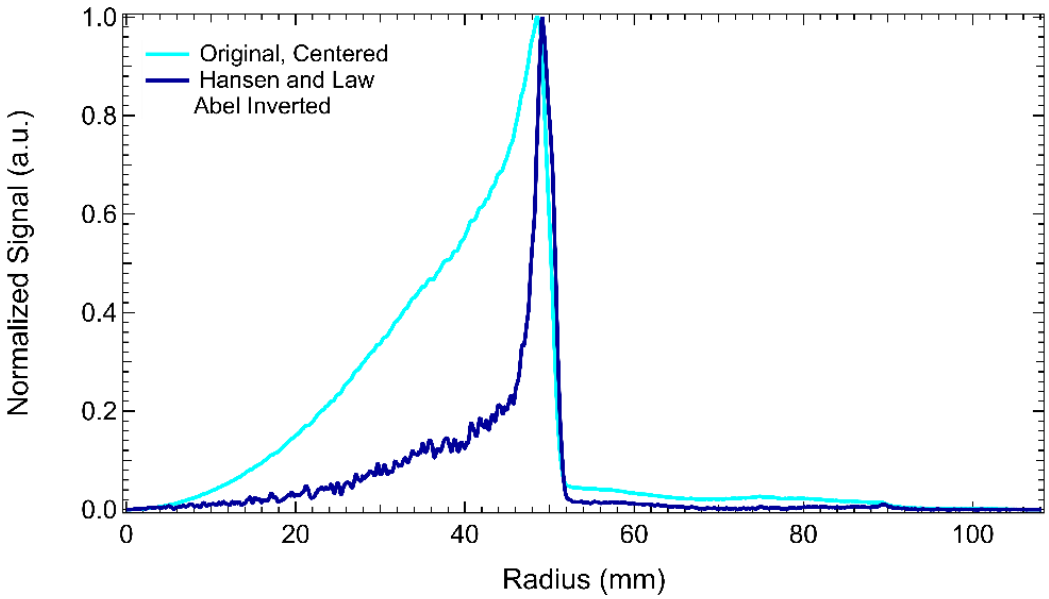

Figure 13:Angular integration profiles for pre- and post-Abel-inverted images. The radial location zero is the center of the flame.

ii. Radical Zone Thickness Time-Histories

A spatial, quantitative analysis can be done with the radial profile of the investigated radical, OH^* or CH^*, to estimate the thickness of the radical zone. For this study the FWHM was decided to estimate the thickness of the radical zone (i.e. the region of highest number density for OH^* and CH^*), and it is the x-axis width of the area at which the y-axis variable is equal to half its maximum value. The exact process of calculating FWHM involved a Python algorithm which extracted the values from the 1D array of normalized y values greater than 0.5, into a smaller array. The beginning and end of the extracted array are slightly greater than 0.5, and the y values located just outside of these extremes are slightly less than 0.5. Using these 4 values and their

corresponding radial locations (x-axis), two interpolations were carried out to estimate the radial positions of 0.5 in the y-values. Recalling that this Abel transform is not exact and is merely a numerical estimation of the 2D radical profile in the slice of the flame volume, no additional information could be inferred regarding the thickness of a single flame image. However, this algorithm was used for a series of flame images to investigate the time history of the radical zone thickness. The implementation of this concept in Python involved evaluating the FWHM for each image in a series of images of a single flame. With the knowledge of the frame rate and the FWHM every 50 μs throughout the propagation, a plot was made of the thickness over time for a single flame propagation experiment, and the differences between radical zone thicknesses were compared for each mixture. A sample of the data is shown for a stoichiometric methane-air flame in Figure 14.

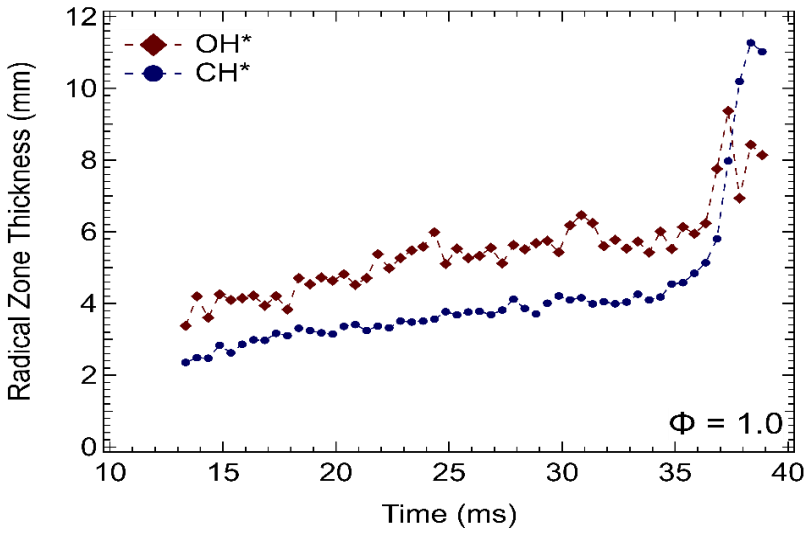

Figure 14: Radical zone thickness time history for stoichiometric methane-air mixture.

The trends show that zone thicknesses grew by about 3 mm until the last few images. The drastic increase in slope at the end of both OH^* and CH^* plots was likely due to part of the flame edge reaching the camera view, because the flame edge did not cross the window edge uniformly. Because of this, the final 4 datapoints of both plots are likely not representative of the flame's radical zone thicknesses, but the points were nonetheless included in the figures to show the effects of irregularities in the data. A collection of the zone thickness plots for the lean and rich mixtures is shown in Figure 15.

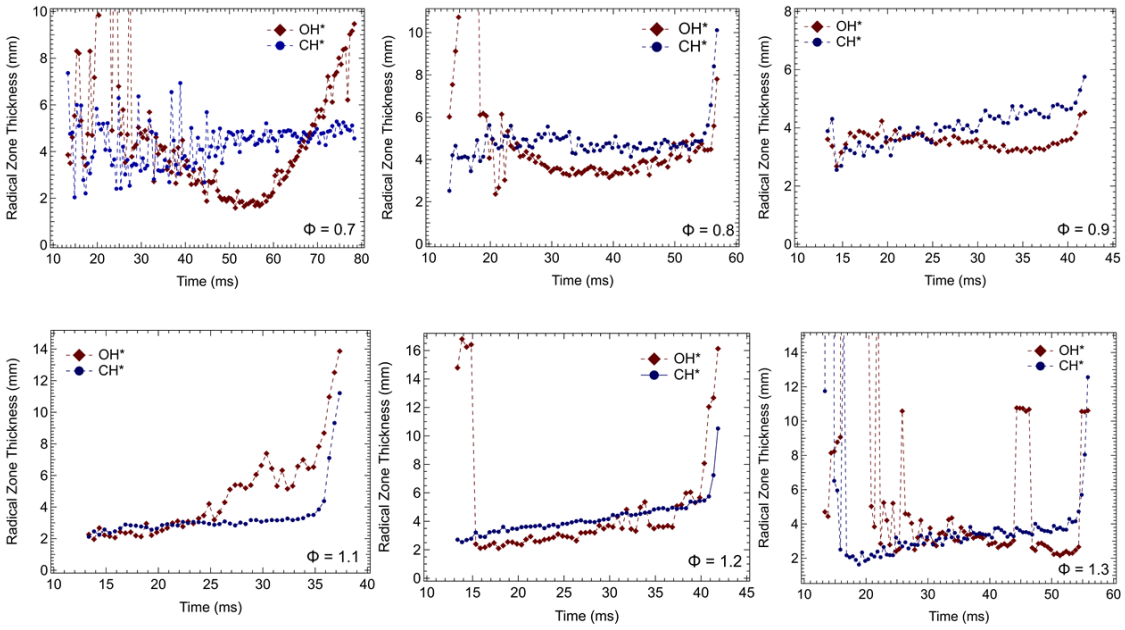

Figure 15: Radical zone thickness plots for lean and rich methane-air mixtures.

There were rapid slope increases within the last few datapoints for each dataset. Again, these can likely be attributed to the flame crossing the edge of the window with respect to the view of the camera. The chemiluminescence signal peaked along with

flame speed (ϕ = 1.1), and leaner and richer flames required higher intensifier gains that reduced the signal-to-noise ratio. This situation, along with non-circular flame profiles, accounted for the fluctuations in the zone thicknesses for 0.7, 0.8, and 1.3 equivalence ratio flames. There was also observed an effect in the flame location due to buoyancy of the lean flames: throughout the lean flame propagation, the flame volume was lifted towards the top of the vessel, and this effect affected the RZT algorithm. The OH^* profile for 0.7 is trough-like and unique in that the thickness decreases until 55 ms, and then the thicknesses rapidly increases to nearly 1 cm. There were other irregularities in the data such as the 5-point spike in OH^* thickness for ϕ = 1.3, and their causes are currently under investigation. For ϕ = 1.0 and 1.1, as shown in Figure 14 and Figure 15, respectively, the OH^* thickness was greater than for CH^*; however, the opposite is true for all other equivalence ratios that were tested.

CHAPTER IV

OH PLANAR LASER-INDUCED FLUORESCENCE

1. Experimental Apparatus

Two lasers are employed to assemble the OH-PLIF imaging system in spherically expanding, laminar and turbulent flames. The first of these two lasers was a solid-state, nanosecond, frequency-doubled, neodymium: yttrium aluminum garnet (Nd:YAG) laser (Spectra-Physics, QuantaRay LAB 130) providing an output at 532 nm wavelength. After the initial warm up, the peak laser energy was 190 mJ/pulse at the 10-Hz repetition rate. The 532-nm output beam was used to pump a tunable dye laser (TDL) (Continuum, ND6000). The TDL dye mixture contained Rhodamine 590 dissolved in methanol (CH_3OH). The output wavelength from TDL was monitored using a wavemeter (HighFinesse, WS7). The tunable dye laser output at 565.500 nm was subsequently frequency-doubled in a beta-barium borate (BBO) crystal to obtain UV radiation in the 282.750 nm wavelength.

The frequency doubled beam outside of the dye laser was transmitted into the experimentation cell. Then the UV beam was guided into the combustion vessel using several dielectric laser mirrors. Sheet-forming optics converted the laser beam into a vertically expanding and horizontally focused sheet, resembling a two-dimensional plane. The sheet-optics consisted of a UV fused silica, planoconcave, cylindrical lens (f = -25 mm, 20x30mm), and a 2”, spherical, planoconvex lens (f = +500 mm) with anti-reflection coating near 283 nm. The optics were placed such that the sheet was focused

at the center of the vessel, and the sheet width at the focus was imaged using a beam profile camera (Ophir, BeamGage) and was estimated to be approximately 290 μm.

According to the LIFBASE software package and previous work [39], the excitation wavelength of the $Q_1(5)$ transition in the OH A←X (1,0) band is at 282.750 nm. A wavelength scan was performed prior to the actual OH-PLIF experiments, to verify the proper laser wavelength. A Hencken calibration burner was configured to produce a stoichiometric methane-air flame, and the laser was tuned across the expected wavelength range. At each wavelength, the BBO crystal was rotated to change the incident beam angle on the face of the crystal, to maintain a fixed 10 mJ/pulse beam energy. For each wavelength scan, an average of 100 consecutive OH-PLIF images was recorded using an intensified charge-coupled device (ICCD) camera (Princeton Instruments, PI-MAX4). From a total integration in both x and y directions of each image, a single value represents the total OH fluorescence signal was obtained at each laser wavelength. This study was used to verify the excitation wavelength of the laser as provided by LIFBASE calculation. Figure 16 provides a sample OH PLIF image, and the plot on the right is generated from the result of the wavelength scan. The peak signal occurs when the laser wavelength is around 282.750 nm, as expected. With the excitation wavelength confirmed, the mobile laser system was moved to the flame speed laboratory for spherically expanding PLIF experiments.

Spherically expanding flames are generated in the vessel placed inside a separate chamber in the flame speed laboratory. In general, high-speed schlieren imaging is used to obtain the propagation of the density gradient, which is then used to obtain the flame

front location for subsequent calculation of the laminar flame speed by many experimental groups [16,17,36]. The most recent facility in the flame speed laboratory is the turbulent flame speed vessel (TFSV), and it contains orthogonal fans for creating known turbulent intensities in the combustible mixture. The vessel also has the capability to produce laminar flames by removing the stirring fans. Morones et al. described the design and construction of the TFSV and studied the turbulent capabilities of the vessel [35]. The most recent studies using the TFSV explored an application of two-dimensional chemiluminescence imaging for measurement of laminar flame speed and species time history data as described in the previous section [20,21]. As detailed by Morones et al., vessel ignition is controlled by an ignition control unit made in-house. The outputs of the ignition control unit include a 12-V power supply and a 5-V trigger, operating an automotive ignition coil. Upon receiving the 5-V trigger pulse, a relay closes, creating a high voltage spark across the electrode tip and the grounding rod centered in the vessel. For these experiments, the ignition coil trigger was created by a delay generator, independent from the ignition control unit.

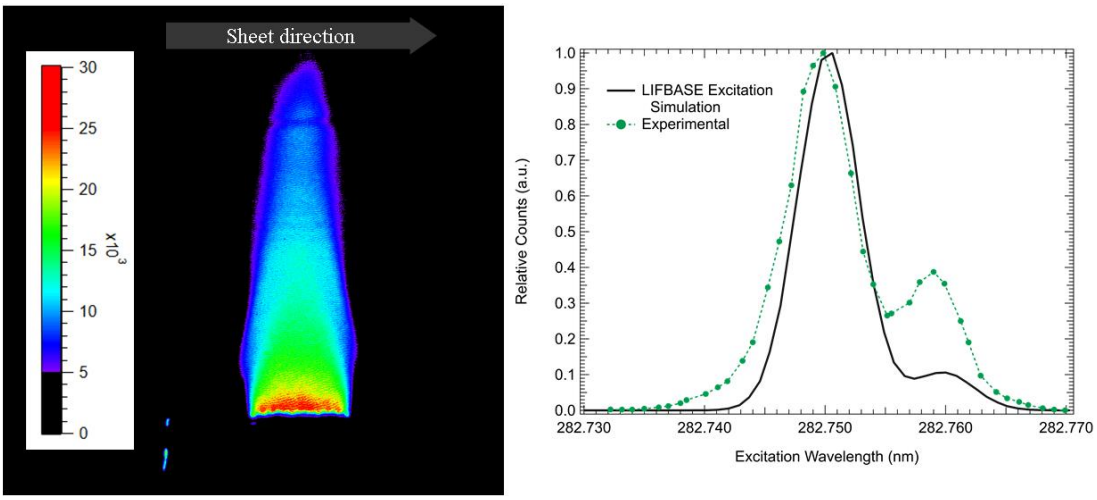

Figure 16: Wavelength scan results as compared to the ideal excitation wavelength as provided by LIFBASE for stoichiometric CH_4-air flame. An example OH PLIF image of the Hencken calibration flame is shown in the left.

The TFSV can produce initial mixture pressures up to 10 atm. Blast-proof walls containing the flame speed vessel protect the operators against explosion accident and the entire facility was remotely operated. Because these studies were conducted in a separate laboratory, it was necessary to build a mobilizing cart for the laser system that enabled the laser to be moved close to the experimentation room for short time durations. The upper of the two levels of the cart supported the laser heads and Nd:YAG control panel, and the remaining room on the upper table was used for the dye laser and mounting the frequency-doubling crystal, as well as optics directing the beam into the test cell containing the flame speed vessel. The lower level held the power supply and cooling system for the Nd:YAG laser and the dye circulator. Figure 17a shows the fully-assembled, mobile laser cart along with the laser system in place.

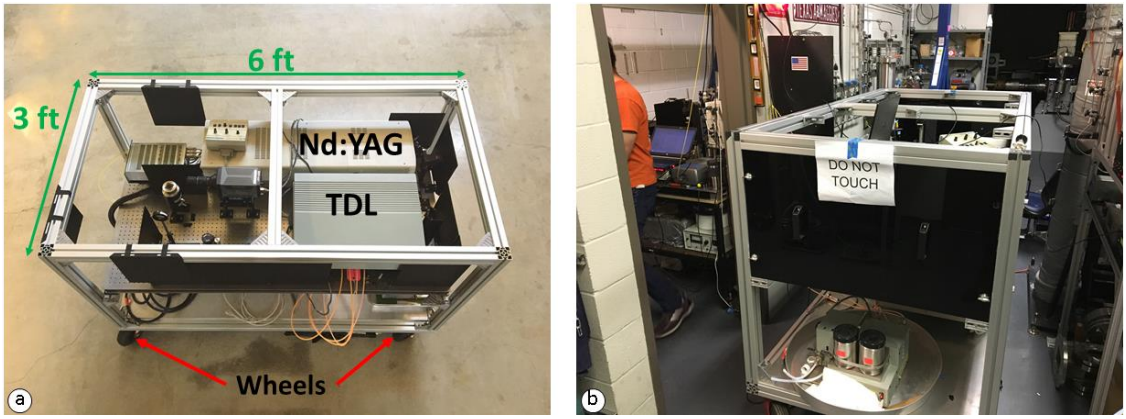

Figure 17: (a) Laser cart with Nd:YAG laser and tunable dye laser. (b) The laser cart parked outside the test cell containing the flame speed vessel to the left of the cart.

The blast walls of the experiment cell are made of rebar-reinforced concrete, and the room was too small to fit the laser cart inside. Because of this, the cart was placed close to the cell wall with the beam parallel to it, as shown in Figure 17b. A hole was drilled through the wall, and by adding a 45-degree, ultraviolet mirror, the beam was passed into the test cell. A periscope elevated the beam to the middle plane of the vessel, and several more ultraviolet mirrors were used to direct the beam into the vessel. The sheet-forming optics created a diverging sheet that passed through one of the vessel windows and in between the pin electrodes. An estimated energy loss was ~10% from the BBO crystal to inside the vessel. This schematic of the entire experimental configuration is illustrated along with other experimental components in Figure 3.

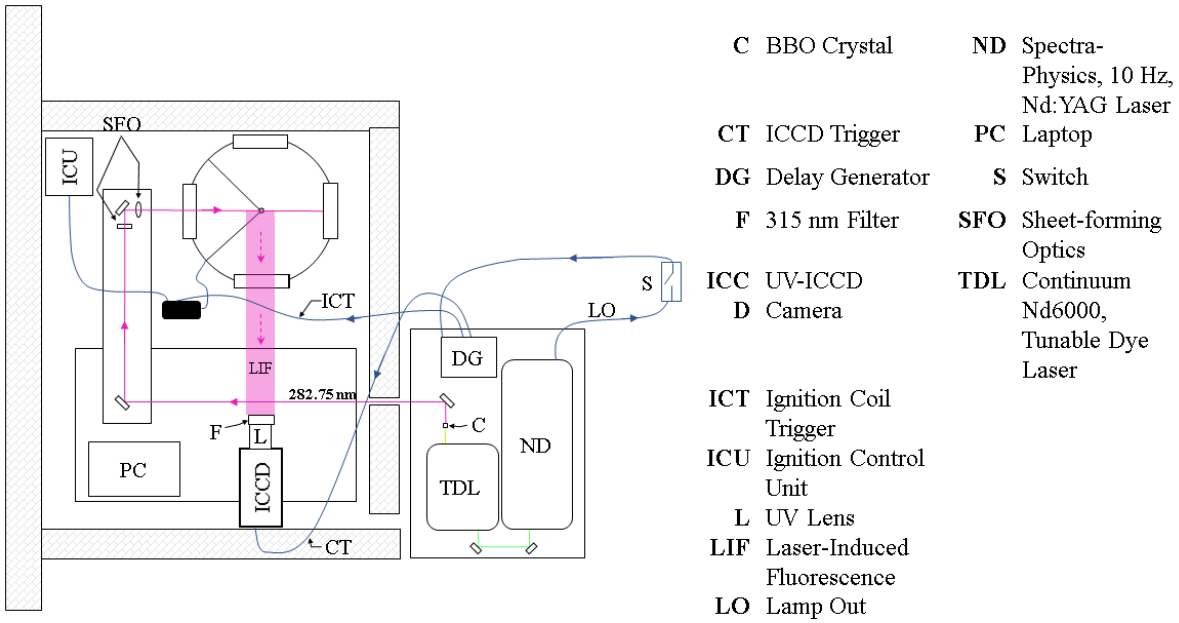

Figure 18: Spherically expanding, OH PLIF experimental configuration.

The ICCD camera contains an external trigger used for single-shot imaging where the master trigger is external to the imaging system. The detector produced 1024x1024 pixel images, providing high-resolution detail of flame structures. This high-resolution capability is particularly useful for complex combustion environments including turbulent combustion at high pressures and high temperatures that are relevant to gas turbine combustors and internal combustion engines. Princeton Instruments software, LightField, was used to control the ICCD gating and other imaging variables. A 500-ns fixed intensifier gate width was used throughout the experiments. Although the laser pulse was only 10 ns, a relatively wide gate provided room for jitter in the laser, delay generator, and internal camera hardware. A gain of 100% was used throughout the experiments, and this made comparison of data easier between different experimental runs. A 45-mm, f/1.8 UV camera lens (Bernhard Halle Nachfl) was mounted on to the

ICCD camera, and a 315-nm bandpass filter (Semrock, FF01-315/15-50) was mounted at the front end of the camera lens to block laser scatter and unwanted flame illumination.

A delay generator (DG) (Stanford Research Systems, DG645) synchronized the laser pulse, ICCD gate, and the vessel ignition, as illustrated in Figure 19. Some variable time, *x*, after the initial pulse, the DG triggered the ignition coil for a duration of 3 ms. A variable ignition time enabled controlling the imaging time during the flame propagation. The ICCD gate opened 200 ns before the rising edge of the laser pulse. As the spherically expanding flame propagated to the vessel walls, the ICCD camera recorded a single-shot resulting in 2D OH-PLIF profile within the flame.

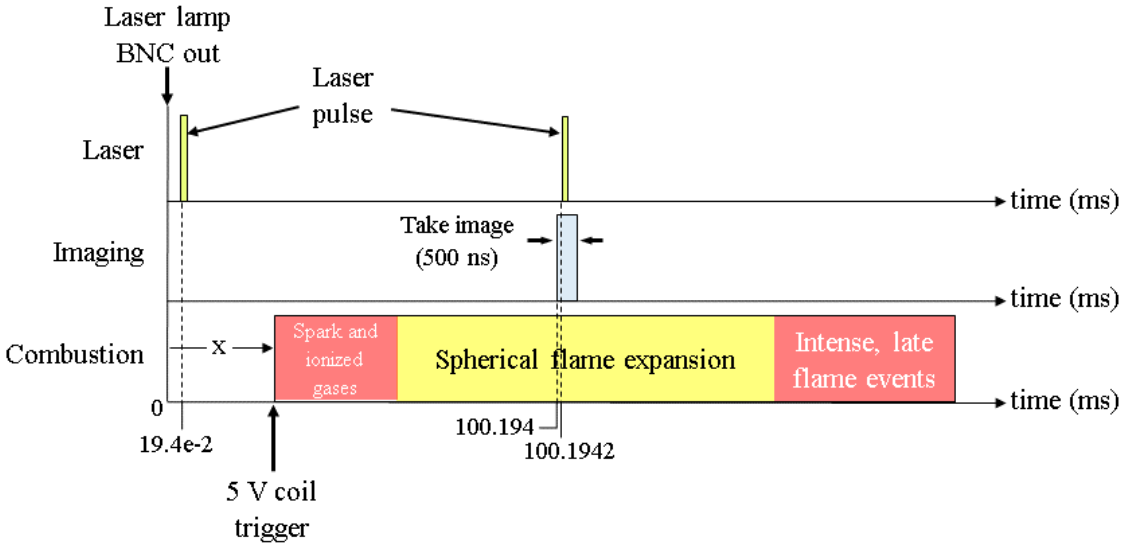

Figure 19: OH PLIF experimental timeline. Variable x controlled the time of the image. From [21]; reprinted by permission of the American Institute of Aeronautics and Astronautics, Inc.

2. Results and Discussion

The results to be discussed in this section consist of three separate experiments: time-series of a stoichiometric mixture, constant-volume flame images across varying

equivalence ratios, and imaging in turbulent flames. Shown in Figure 20 are the uncorrected OH PLIF images resulting from incrementing *x* (Figure 19) by 2 ms steps until the flame had propagated past the observation window. This flame was produced from a stoichiometric (ϕ = 1.0) CH_4 + air (O_2 + 3.76N_2) mixture. The initial pressure and temperature were 1 atm and 300 K, respectively. In the middle of the frame on the left half, one of the ignition electrodes can be visible, and the other grounding electrode is located behind that electrode. The laser sheet passed through the window on the left side, through the flame from left to right. It is necessary to note that because each experiment provides one resulting image, each of these images was acquired in a separate, sequential experiment.

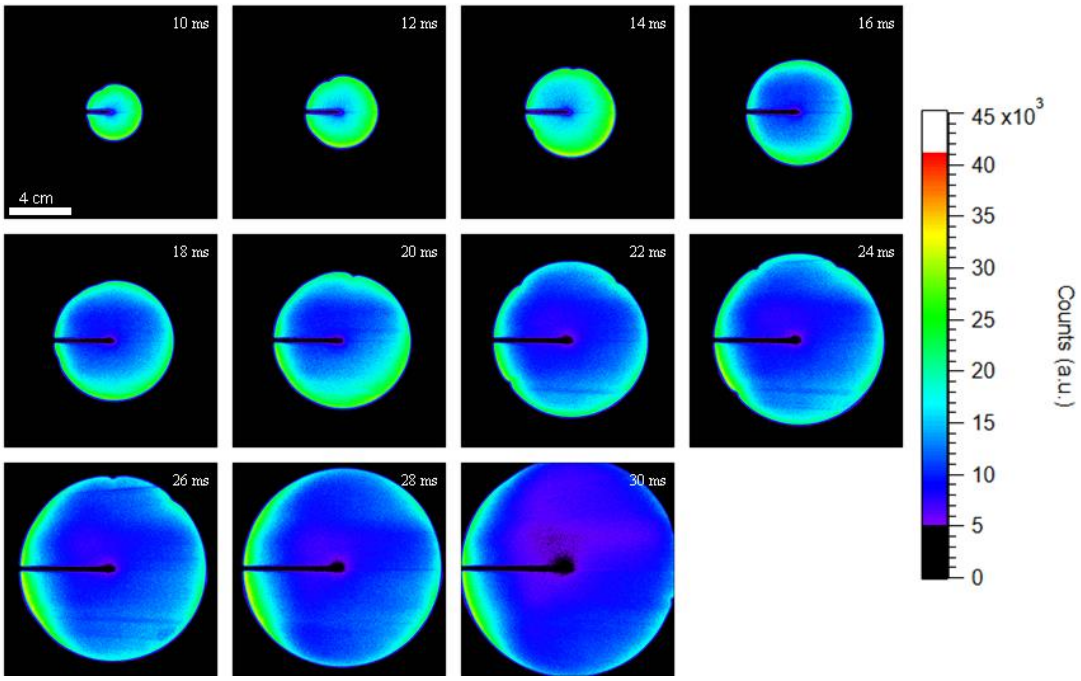

Figure 20: Time-series of OH PLIF images in a stoichiometric methane-air mixture at 1 atm pressure.

These images indicate a higher OH distribution towards the beginning of combustion. The PLIF images shown are not corrected for irregularities in the laser sheet as well as quenching and fluorescence trapping. Subsequently, PLIF signal are calibrated using the Hencken calibration burner operated inside the flame speed vessel. A series of PLIF images like these are like those produced in high-speed chemiluminescence measurements mentioned previously, however, the PLIF images corresponding to a specific 2D plane and can be especially significant in the case of turbulent flames. The OH PLIF data can provide the necessary information to calculate laminar flame speed as well as time-resolved species information for chemical kinetics model development in laminar and turbulent flames.

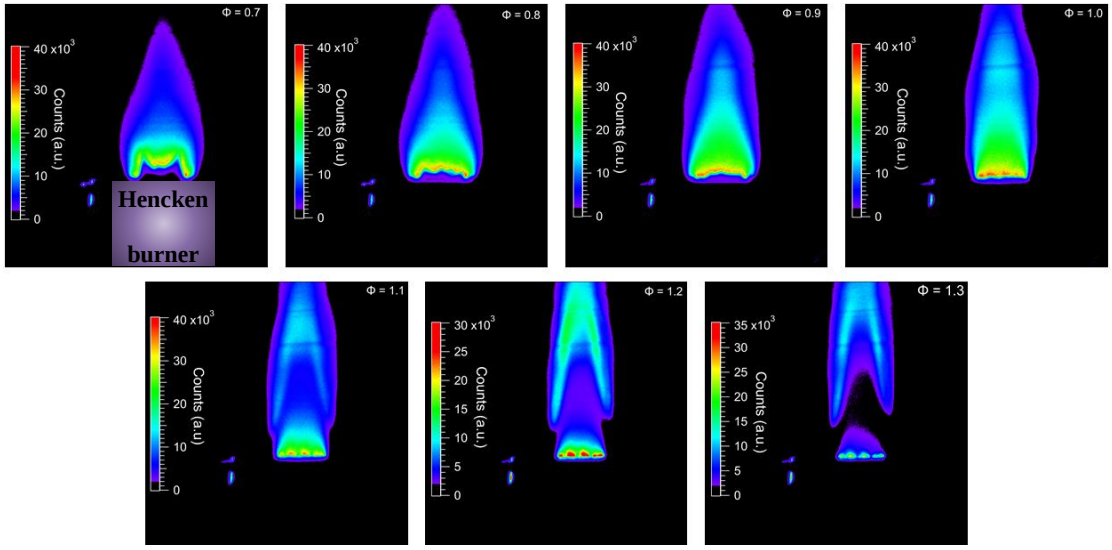

Figure 21: Hencken calibration flame images as a function of the equivalence ratio.

To quantitatively analyze OH PLIF images, calibration was performed using a Hencken calibration burner. With a flame lifted above the burner surface and with a shroud gas that reduce flame instabilities, the Hencken flame was assumed be adiabatic.

The central regions of the Hencken burner flames shown in Figure 21 were used for equilibrium calculations (5-25 mm above the burner surface), and the average counts within the equilibrium region were correlated to OH number densities for the same mixture using the STANJAN equilibrium code. The calibration burner was configured such that it could be probed within the flame speed vessel, and the flame images acquired have the same excitation and detection efficiency of the spherically expanding flames. Calibration images were acquired for the full range of equivalence ratios used in the experiments, and at varying heights in the burner to account for changes in the beam profile. There are clear instabilities and non-uniformities in the lean and rich flames, and these may cause some uncertainty in the results when estimating the area of equilibrium within only a 20 mm x 17 mm region of the Hencken flames.

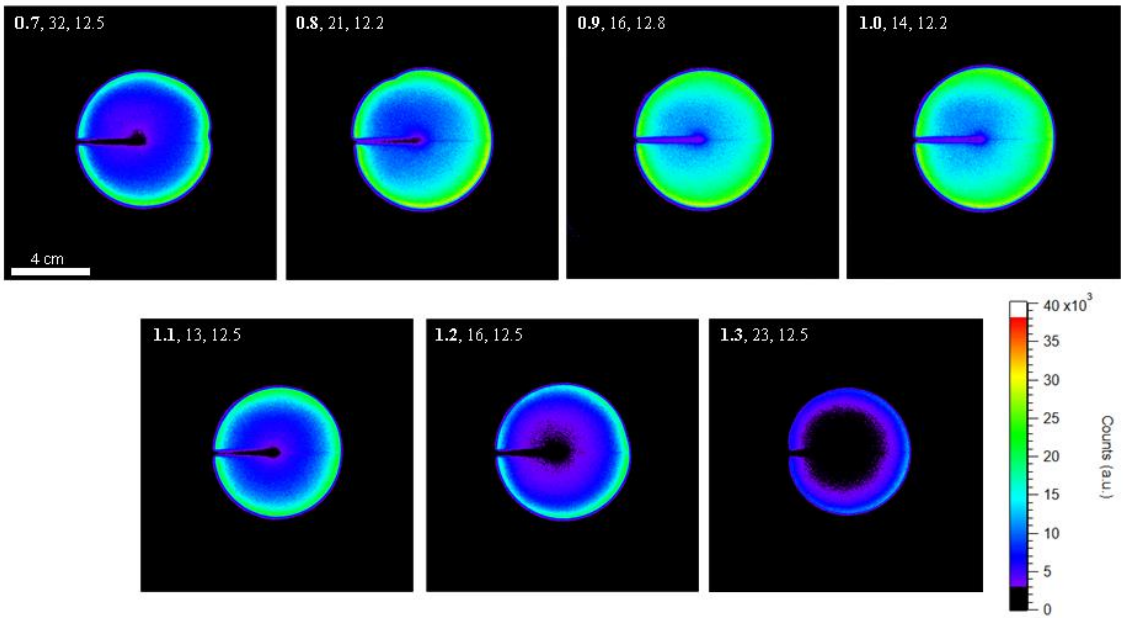

Figure 22: Constant-radius flame images taken from individual OH PLIF experiments. In the upper left of each image, the list of values indicates ϕ, time after ignition (ms), and beam energy (mJ).

The second set of images were acquired with the aim of comparing OH number density as a function of equivalence ratio, and the results are shown in Figure 22. One consideration for these data are that equilibrium conditions can be only present in the middle post flame region, and close to the outer diameter a state of non-equilibrium can be present. Hence typical OH PLIF images like these can provide extremely valuable information for flame modelers. Another important aspect of these images is that the flames are of similar diameter and can be used to compare the flame front location and OH distribution profile as a function of flame equivalence ratio. Upon visual inspection, peak OH-PLIF signal is found to be located between ϕ =0.9 and 1.0, and the concentration tapers on either side of the peak. This OH profile appears to have a slightly greater gradient for rich mixtures as compared to the lean ones.

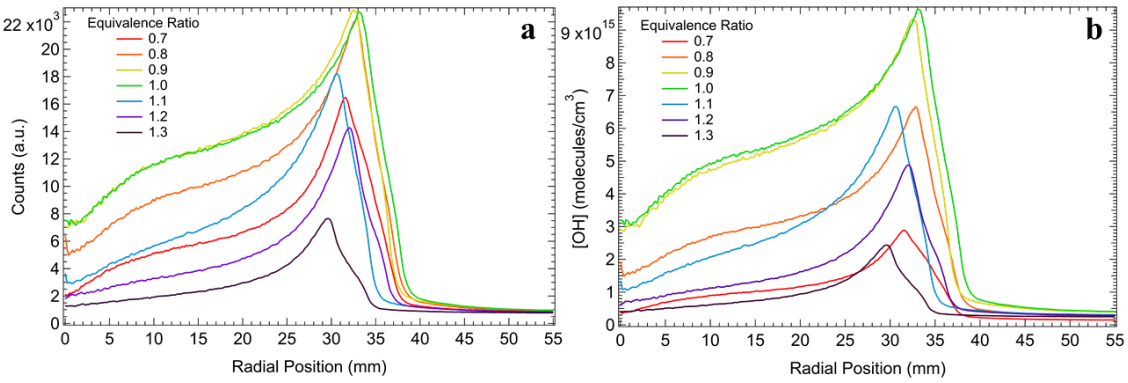

Figure 23: (a) Image counts as a function of the radial position. (b) Corresponding OH number densities after implementing calibration flame data and STANJAN equilibrium calculations as discussed in the text.

With the Hencken burner OH-PLIF images, and equilibrium data for OH concentration, a ratio was derived resulting in OH number density per pixel count. This ratio is applied to the raw radial intensity profiles shown in Figure 23a obtained from the images in Figure 22, resulting in calibrated OH number density profiles, as shown in

Figure 23b. The rich data shown here can be critical for validation laminar flame models and will be discussed in separate publications.

To demonstrate OH PLIF imaging in turbulent flames, the orthogonal stirring fans were installed in the vessel to stir the mixture and induce turbulent flow. Because the ignition control unit controlled the timing between the fan motors and the ignition spark, and that for these experiments the ignition coil was triggered externally, the control unit could not repeatably turn on the fans at the same time before each ignition. For this reason, the fans were turned on several seconds prior to ignition, spinning at 2000 rpm, and remained on during the combustion process. These flames are simply some representative cases present in practical combustors, and these experiments can reveal flame features undetectable by simple chemiluminescence imaging.

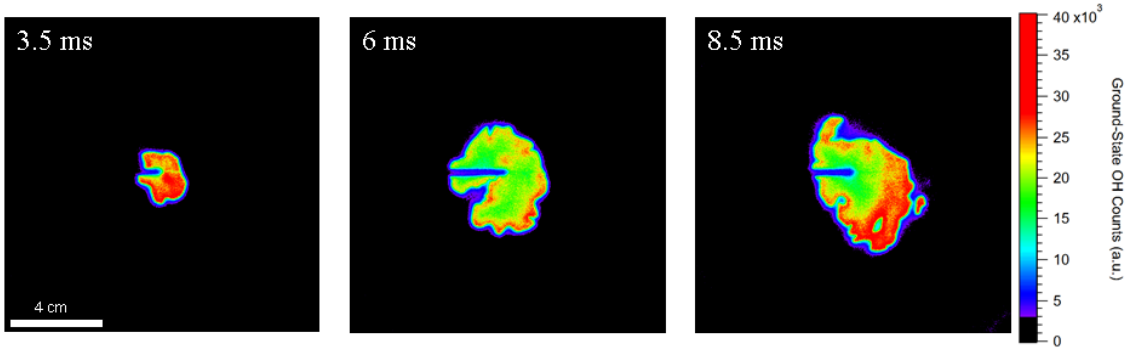

Figure 24: OH PLIF images in sample turbulent flames recorded from three individual experiments. The time indicated on each image is the time after ignition.

CHAPTER V

CONCLUSIONS

1. Chemiluminescence Imaging

The first part of this thesis research was devoted to developing high-speed chemiluminescence-based diagnostics for spherically expanding flames. The objective was to obtain time-resolved species time histories during the flame propagation as well as to compare the laminar flame speed calculations against commonly used schlieren-based imaging method. This work utilized a repeatable apparatus for 2D chemiluminescence imaging of OH^* and CH^* in spherically expanding flames to expand the dimensionality of data reduction when compared to the schlieren method for laminar flame speed measurements. The data recorded were used for laminar flame speed calculations and agree well with previous schlieren-based results. In addition to simply obtaining only the flame speed, the Hansen and Law Abel inversion was applied to obtain the species-specific images. Angular integrations were performed to estimate the radical zone thickness. Time-histories of the RZT calculations showed there is a need for improvements in the data quality. One suggestion for improvement is an increase in the signal-to-noise ratio. This could be improved by elimination of a mirror that may absorb some of the flame emission. Another improvement would be generation of more spherically uniform flames, and this can be done by reducing the spark gap and making sure that the electrodes are flat and lie within the same plane. The chemiluminescence data is line-of-sight averaged and lack spatial resolution, and therefore they can only be used to obtain one-dimensional species time histories to Abel inversion only when

perfect cylindrical symmetry can be assumed. Therefore, more advanced planar imaging is required for turbulent flame conditions relevant to realistic combustion hardware, leading to the laser-based PLIF imaging development performed subsequently.

2. Hydroxyl Planar Laser-Induced Fluorescence

Time-resolved OH PLIF images of spherically expanding methane-air flames can be used for laminar flame speed calculations as well as validation of numerical flame models with full chemical kinetics mechanisms during future work. The laminar flame data that resulted from this work will be useful for developing time histories of OH concentration distribution as well as comparison between experiments of varying equivalence ratios. Constant-volume, calibrated OH-PLIF images show differences in the OH gradient profiles between lean and rich conditions, however, the primary application of OH PLIF becomes critical in turbulent flame conditions as described above. As a proof-of-principle demonstration, relative OH concentration images were detected in turbulent flames, and these data reveal fine details of flame features that may not be resolved by simple chemiluminescence imaging. Future work will include more detailed experiments under known turbulent intensities. The turbulent data are particularly useful for a more fundamental study of the turbulent flames that occur in the most practical engines. Future work will also investigate excitation of other radicals such as CH radical to compare with previous chemiluminescence experiments and generate rich data sets of 2D time-resolved radical concentrations for chemical kinetics studies of various practical fuels and fuel blends.

REFERENCES

[1] Maeda, K., Wall, M. L., and Carr, L. D., "Hyperfine structure of the hydroxyl free radical (OH) in electric and magnetic fields," *New Journal of Physics*, vol. 17, Apr. 2015, p. 045014.

[2] Carlone, C., and Dalby, F. W., "Spectrum of the hydroxyl radical," *Canadian Journal of Physics*, vol. 47, Sep. 1969, pp. 1945–1957.

[3] Bennett, R. G., and Dalby, F. W., "Experimental Determination of the Oscillator Strength of the Violet System of OH," *The Journal of Chemical Physics*, vol. 40, Mar. 1964, pp. 1414–1416.

[4] Egolfopoulos, F. N., Hansen, N., Ju, Y., Kohse-Höinghaus, K., Law, C. K., and Qi, F., "Advances and challenges in laminar flame experiments and implications for combustion chemistry," *Progress in Energy and Combustion Science*, vol. 43, Aug. 2014, pp. 36–67.

[5] Jayachandran, J., Zhao, R., and Egolfopoulos, F. N., "Determination of laminar flame speeds using stagnation and spherically expanding flames: Molecular transport and radiation effects," *Combustion and Flame*, vol. 161, Sep. 2014, pp. 2305–2316.

[6] Jayachandran, J., Lefebvre, A., Zhao, R., Halter, F., Varea, E., Renou, B., and Egolfopoulos, F. N., "A study of propagation of spherically expanding and counterflow laminar flames using direct measurements and numerical simulations," *Proceedings of the Combustion Institute*, vol. 35, 2015, pp. 695–702.

[7] Bosschaart, K. J., and de Goey, L. P. H., "The laminar burning velocity of flames propagating in mixtures of hydrocarbons and air measured with the heat flux method," *Combustion and Flame*, vol. 136, Feb. 2004, pp. 261–269.

[8] Van Maaren, A., Thung, D. S., and De Goey, L. R. H., "Measurement of Flame Temperature and Adiabatic Burning Velocity of Methane/Air Mixtures," *Combustion Science and Technology*, vol. 96, Jan. 1994, pp. 327–344.

[9] Davis, S. G., and Law, C. K., "Determination of and Fuel Structure Effects on Laminar Flame Speeds of C $_1$ to C $_8$ Hydrocarbons," *Combustion Science and Technology*, vol. 140, Dec. 1998, pp. 427–449.

[10] Vagelopoulos, C. M., Egolfopoulos, F. N., and Law, C. K., "Further considerations on the determination of laminar flame speeds with the counterflow twin-flame technique," *Symposium (International) on Combustion*, vol. 25, Jan. 1994, pp. 1341–1347.

[11] Jomaas, G., Zheng, X. L., Zhu, D. L., and Law, C. K., "Experimental determination of counterflow ignition temperatures and laminar flame speeds of C2–C3 hydrocarbons at atmospheric and elevated pressures," *Proceedings of the Combustion Institute*, vol. 30, Jan. 2005, pp. 193–200.

[12] Wu, F., Kelley, A. P., and Law, C. K., "Laminar flame speeds of cyclohexane and mono-alkylated cyclohexanes at elevated pressures," *Combustion and Flame*, vol. 159, Apr. 2012, pp. 1417–1425.

[13] Kelley, A. P., and Law, C. K., "Nonlinear effects in the extraction of laminar flame speeds from expanding spherical flames," *Combustion and Flame*, vol. 156, Sep. 2009, pp. 1844–1851.

[14] Dowdy, D. R., Smith, D. B., Taylor, S. C., and Williams, A., "The use of expanding spherical flames to determine burning velocities and stretch effects in hydrogen/air mixtures," *Symposium (International) on Combustion*, vol. 23, Jan. 1991, pp. 325–332.

[15] Chen, Z., "On the accuracy of laminar flame speeds measured from outwardly propagating spherical flames: Methane/air at normal temperature and pressure," *Combustion and Flame*, vol. 162, Jun. 2015, pp. 2442–2453.

[16] de Vries, J., Lowry, W. B., Serinyel, Z., Curran, H. J., and Petersen, E. L., "Laminar flame speed measurements of dimethyl ether in air at pressures up to 10atm," *Fuel*, vol. 90, Jan. 2011, pp. 331–338.

[17] Sikes, T., Mannan, M. S., and Petersen, E. L., "An experimental study: laminar flame speed sensitivity from spherical flames in stoichiometric CH_4 –air mixtures," *Combustion Science and Technology*, vol. 190, Sep. 2018, pp. 1594–1613.

[18] Lamoureux, N., Djebaïli-Chaumeix, N., and Paillard, C.-E., "Laminar flame velocity determination for H2–air–He–CO2 mixtures using the spherical bomb method," *Experimental Thermal and Fluid Science*, vol. 27, Apr. 2003, pp. 385–393.

[19] Gu, X. J., Haq, M. Z., Lawes, M., and Woolley, R., "Laminar burning velocity and Markstein lengths of methane–air mixtures," *Combustion and Flame*, vol. 121, Apr. 2000, pp. 41–58.

[20] Turner, M. A., Parajuli, P., Paschal, T., Kulatilaka, W. D., and Petersen, E. L., "Laminar Flame Speed Measurements from Chemiluminescence of OH* and CH* in CH_4-Air Flames," *AIAA Scitech 2019 Forum*, San Diego, California: American Institute of Aeronautics and Astronautics, 2019.

[21] Paschal, T., Parajuli, P., Turner, M. A., Petersen, E. L., and Kulatilaka, W. D., "High-Speed OH* and CH* Chemiluminescence Imaging and OH Planar Laser-Induced Fluorescence (PLIF) in Spherically Expanding Flames," *AIAA Scitech 2019 Forum*, San Diego, California: American Institute of Aeronautics and Astronautics, 2019.

[22] Hanson, R. K., "Planar laser-induced fluorescence imaging," *Journal of Quantitative Spectroscopy and Radiative Transfer*, vol. 40, Sep. 1988, pp. 343–362.

[23] Allen, M. G., and Hanson, R. K., "Planar Laser-Induced-Fluorescence Monitoring Of OH In A Spray Flame," *Optical Engineering*, vol. 25, Dec. 1986.

[24] Aleiferis, P. G., and Rosati, M. F., "Flame chemiluminescence and OH LIF imaging in a hydrogen-fuelled spark-ignition engine," *International Journal of Hydrogen Energy*, vol. 37, Jan. 2012, pp. 1797–1812.

[25] Sakakibara, J., and Adrian, R. J., "Whole field measurement of temperature in water using two-color laser induced fluorescence," *Experiments in Fluids*, vol. 26, Jan. 1999, pp. 7–15.

[26] Singla, G., Scouflaire, P., Rolon, C., and Candel, S., "Planar laser-induced fluorescence of OH in high-pressure cryogenic LOx/GH2 jet flames," *Combustion and Flame*, vol. 144, Jan. 2006, pp. 151–169.

[27] Hanson, R. K., Seitzman, J. M., and Paul, P. H., "Planar laser-fluorescence imaging of combustion gases," *Applied Physics B Photophysics and Laser Chemistry*, vol. 50, Jun. 1990, pp. 441–454.

[28] Tanahashi, M., Murakami, S., Choi, G.-M., Fukuchi, Y., and Miyauchi, T., "Simultaneous CH–OH PLIF and stereoscopic PIV measurements of turbulent premixed flames," *Proceedings of the Combustion Institute*, vol. 30, Jan. 2005, pp. 1665–1672.

[29] Sadanandan, R., Stöhr, M., and Meier, W., "Simultaneous OH-PLIF and PIV measurements in a gas turbine model combustor," *Applied Physics B*, vol. 90, Mar. 2008, pp. 609–618.

[30] Donbar, J. M., Driscoll, J. F., and Carter, C. D., "Reaction zone structure in turbulent nonpremixed jet flames—from CH-OH PLIF images," *Combustion and Flame*, vol. 122, Jul. 2000, pp. 1–19.

[31] Locke, R. J., Hicks, Y. R., Anderson, R. C., and Ockunzzi, K. A., "OH imaging in a lean burning high-pressure combustor," *AIAA Journal*, vol. 34, Mar. 1996, pp. 622–624.

[32] Allen, M. G., McManus, K. R., Sonnenfroh, D. M., and Paul, P. H., "Planar laser-induced-fluorescence imaging measurements of OH and hydrocarbon fuel fragments in high-pressure spray-flame combustion," *Applied Optics*, vol. 34, Sep. 1995, p. 6287.

[33] Frank, J., Miller, M., and Allen, M., “Imaging of laser-induced fluorescence in a high-pressure combustor,” *37th Aerospace Sciences Meeting and Exhibit*, Reno,NV,U.S.A.: American Institute of Aeronautics and Astronautics, 1999.

[34] Laufer, G., Quagliaroli, T. M., Krauss, R. H., Whitehurst, III, R. B., McDaniel, J. C., and Grinstead, J. H., “Planar OH density and apparent temperature measurements in a supersonic combusting flow,” *AIAA Journal*, vol. 34, Mar. 1996, pp. 463–469.

[35] Morones, A., Leon, V. J., and Petersen, E. L., “Reconfigurable Fan-Stirred Flame Bomb with Optical Access,” *55th AIAA Aerospace Sciences Meeting*, Grapevine, Texas: American Institute of Aeronautics and Astronautics, 2017.

[36] Lowry, W., de Vries, J., Krejci, M., Petersen, E., Serinyel, Z., Metcalfe, W., Curran, H., and Bourque, G., “Laminar Flame Speed Measurements and Modeling of Pure Alkanes and Alkane Blends at Elevated Pressures,” *Volume 2: Combustion, Fuels and Emissions, Parts A and B*, Glasgow, UK: ASME, 2010, pp. 855–873.

[37] Hansen, E. W., and Law, P.-L., “Recursive methods for computing the Abel transform and its inverse,” *Journal of the Optical Society of America A*, vol. 2, Apr. 1985, p. 510.

[38] Gibson, S., Danhickstein, Yurchak, R., Dhrubajyoti Das, Shih, G., Furii, Ellisje624, and PhantomYuan, “Pyabel/Pyabel: Pyabel 0.7.6,” Jan. 2017.

[39] Kulatilaka, W. D., Hsu, P. S., Gord, J. R., and Roy, S., “Point and planar ultraviolet excitation/detection of hydroxyl-radical laser-induced fluorescence through long optical fibers,” *Optics Letters*, vol. 36, May 2011, p. 1818.

APPENDIX A

IMAGE PROCESSING PYTHON CODE

```
def flame_thickness(images = [], imageIndex = 20, individual = False, fileType =
'.png', saveDir = '', save=False, show=False, method= u'com', normalize=True):
    '''Two options: 1. Individual image analysis which compares centering methods (com,
convolution, and slice)
                    2. Get flame thickness for an image & display nothing. This is used
when analyzing an array of images at once.

    Keyword arguments:
    images -- <list> --array of images. at this moment, it is not used anywhere (Feb.
2019)
    imageIndex -- <int> -- index of analyzed image in array
    individual -- <bool> -- if True, typically when analyzing one image at a time, will
compare various centering methods
    fileType -- <str> --file extensions of analyzed images, typically .png or .tif
    saveDir -- <str> -- location of saving analysis. used only when individual is True
    show -- <bool> -- when True, displays figures. only used when individual is True
    method -- <str> -- centering method: 'com', 'convolution', or 'slice'. only used
when individual is False
    normalize -- <bool> -- normalize y values (intenisty) when True

    Returns:
    *when individual == False:
        - Thickness of the flame
    '''
    print saveDir
    if not images:
        images = glob.glob('*' + fileType)
    if type(0) == type(imageIndex):
        image = images[imageIndex]
    else:
        image = imageIndex
    try:
        from center import centerPix
        centerRow = centerPix[0]
        centerCol = centerPix[1]
    except:
        centerRow = int(imread(image, as_gray=True).shape[0]/2)
        centerCol = int(imread(image, as_gray=True).shape[1]/2)
        if individual:
            print 'Center file does not exist ==> Default center used (row, col): ' +
'[{},{}]'.format(centerRow,centerCol)
    try:
        import PPI
        if individual:
            print 'Pixels per inch from file: ' + str(PPI.ppi)
        ppi = PPI.ppi
        ppi = ppi/25.4 #ppi to ppmm
    except:
        if individual:
            print sys.exit('PPI file does not exist. Create \"PPI.py\" file with
variable ppi in the directory of these images then try again.')
    if individual:
        gray0 = imread(images[0], as_gray=True) # Used if subtracting to negate
background and bright center
        gray = imread(image, as_gray=True)
        # matplotlib.rcParams.update({'font.size': 22}) # Uncomment to change universal
font size of figures
```

```
        # gray = np.subtract(gray, gray0)
        # gray[gray < 0] = 0 # Set all values less than zero equal to zero
        plt.imshow(gray)
        plt.axvline(int(gray.shape[1]/2),color='r',linestyle=':')
        plt.axhline(int(gray.shape[0]/2),color='r',linestyle=':')
        if saveDir:
            cwd = os.getcwd()
            os.chdir(saveDir)
            plt.savefig('original.png')
            os.chdir(cwd)
        if show:
            plt.show()
        plt.gcf().clear()
        # plt.show()
        x0,y0 = abel.tools.vmi.angular_integration(gray,dr=0.5)
        method1 = u'com'
        method2 = u'convolution'
        method3 = u'slice'

        com, x1, y1 = ImageProcessing.center_image(gray, center=method1, save=save,
saveDir = saveDir, show=show)
        conv, x2, y2 = ImageProcessing.center_image(gray, center=method2, save=save,
saveDir = saveDir, show=show)
        slice, x6, y6 = ImageProcessing.center_image(gray, center=method3, save=save,
saveDir=saveDir, show=show)
        x00 = x0
        x10 = x1
        x20 = x2
        y00 = y0
        y10 = y1
        y20 = y2
        x60 = x6
        y60 = y6
        x0 = np.true_divide(x0,ppi)
        x1 = np.true_divide(x1, ppi)
        x2 = np.true_divide(x2, ppi)
        x6 = np.true_divide(x6,ppi)
        if normalize:
            y0 = np.true_divide(y0,max(y0))
            y1 = np.true_divide(y1, max(y1))
            y2 = np.true_divide(y2, max(y2))
            y6 = np.true_divide(y6,max(y6))

        plt.plot(x0,y0,x1,y1,x2,y2,x6,y6)
        plt.title('Center Methods')
        plt.xlabel('Radial Position (mm)')
        plt.ylabel('Normalized Signal')
        plt.legend(['original', method1, method2, method3])
        if saveDir:
            cwd = os.getcwd()
            os.chdir(saveDir)
            plt.savefig('center_methods.png')
            wbk = xlsxwriter.Workbook('Center Methods' + '.xlsx')
            wks = wbk.add_worksheet()
            wks.write_column(0,0,x00)
            wks.write_column(0,1,y00)
            wks.write_column(0,2,x10)
```

```
            wks.write_column(0,3,y10)
            wks.write_column(0,4,x20)
            wks.write_column(0,5,y20)
            wks.write_column(0,6,x60)
            wks.write_column(0,7,y60)
            wbk.close()
            os.chdir(cwd)
        if show:
            plt.show()
        plt.gcf().clear()

        hansenOG, x3, y3 = ImageProcessing.transform_image(gray, center='original',
show=show, save=save,saveDir=saveDir)
        hansenCOM, x4, y4 = ImageProcessing.transform_image(com,center=method1,
show=show, save=save,saveDir=saveDir)
        hansenCON, x5, y5 = ImageProcessing.transform_image(conv,center=method2,
show=show, save=save,saveDir=saveDir)
        hasenSLICE, x7, y7 = ImageProcessing.transform_image(slice, center=method3,
show=show, save=save, saveDir=saveDir)
        x30 = x3
        x40 = x4
        x50 = x5
        x70 = x7
        y30 = y3
        y40 = y4
        y50 = y5
        y70 = y7

        x3 = np.true_divide(x3,ppi)
        x4 = np.true_divide(x4, ppi)
        x5 = np.true_divide(x5, ppi)
        x7 = np.true_divide(x7,ppi)
        if normalize:
            y3 = np.true_divide(y3,max(y3))
            y4 = np.true_divide(y4, max(y4))
            y5 = np.true_divide(y5, max(y5))
            y7 = np.true_divide(y7,max(y7))
        plt.plot(x3,y3,x4,y4,x5,y5,x7,y7)
        plt.title('Hansen Law with Different Centers')
        plt.xlabel('Radial Position (mm)')
        plt.ylabel('Normalized Signal')
        plt.legend(['original', method1, method2,method3])
        if saveDir:
            cwd = os.getcwd()
            os.chdir(saveDir)
            plt.savefig('hansen_center_methods.png')
            wbk = xlsxwriter.Workbook('Hansen Center Methods' + '.xlsx')
            wks = wbk.add_worksheet()
            wks.write_column(0,0,x30)
            wks.write_column(0,1,y30)
            wks.write_column(0,2,x40)
            wks.write_column(0,3,y40)
            wks.write_column(0,4,x50)
            wks.write_column(0,5,y50)
            wks.write_column(0,6,x70)
            wks.write_column(0,7,y70)
            wbk.close()
```

```
            os.chdir(cwd)
        if show:
            plt.show()
        plt.gcf().clear()

    else:
        gray = imread(image, as_gray=True)
        centered, xc, yc = ImageProcessing.center_image(gray, center=method,
save=False, saveDir = saveDir, show=False) # show and save are False default because it
is not a good idea to show and save each of 100+ images for a series, although it could
be done by changing these parameters and entering the peroper save directory
        transformed, xt, yt = ImageProcessing.transform_image(centered, center=method,
show=False, save=False, saveDir=saveDir) # same logic as above
        xt = np.true_divide(xt, ppi)
        norm=False
        if normalize:
            yt = np.true_divide(yt, max(yt))
            norm=True
        return ImageProcessing.get_thickness(xt,yt,norm)
```